Texas A&M University
Mechanical Engineering Department
Turbomachinery laboratory

Squeeze Film Damper with Mechanical Seal: Identification of Force Coefficients from Circular Centered Orbit Tests

Research Progress Report to the Turbomachinery Research Consortium

TRC-SFD-1-06

Luis San Andrés
Mast-Childs Professor
Principal Investigator

Adolfo Delgado
Research Assistant

June 2006

Executive Summary

Air ingestion and entrapment reduce significantly the damping capability of squeeze film dampers. This phenomenon is pervasive in squeeze film dampers with open ends or poor end seals. This report extends the experimental study of a SFD featuring a mechanical seal that effectively eliminates lubricant side leakage. The test damper reproduces an aircraft application intended to contain the lubricant in the film lands for extended periods of time. The test damper journal is 2.54 cm in length and 12.7 cm in diameter, with a nominal clearance of 0.127 mm. The SFD feed end is flooded with oil, while the discharge end contains a recirculation groove and four orifice discharge ports. In a prior 2005 TRC report, single frequency - unidirectional load excitation tests were conducted, without and with lubricant in the squeeze film lands, to determine the seal dry-friction force and viscous damping force coefficients. Presently, tests with single frequency excitation loads rendering circular centered orbits excitations are conducted to identify the test system and SFD force coefficients. The tests include two sets of flow restrictors with orifice sizes equal to 2.8 mm and 1.1 mm in diameter. The flow restrictors regulate the discharge flow area, and thus control the oil flow through the squeeze film damper land. Magnitudes of dynamic pressures in the squeeze film land are similar for both sets of flow restrictors. The measurements also show dynamic pressures in the discharge groove, and with magnitudes more pronounced for small amplitude orbits when compared to the squeeze film land pressures. The identified parameters include the test system damping and the individual contributions from the squeeze film, dry friction in the mechanical seal and structure remnant damping. The identified system damping coefficients are frequency and motion amplitude dependent due to the dry friction interaction at the mechanical seal interface. Identified squeeze film force coefficients, damping and added mass, are in agreement with predictions based on the full film, short length open ends damper model. The experimental squeeze film damper force coefficients are nearly identical for both flow restrictor sizes and for the largest orbit amplitude tested (50 μm).

Table of Contents

List of Tables

List of Figures

Nomenclature

c	Bearing radial clearance [m]
C_d	Empirical orifice discharge coefficient [-]
C_{rv}	Structure remnant damping coefficient [N.s/m]
C_{seal}	Equivalent viscous damping for mechanical seal [N.s/m]
$C_{s\text{-}\alpha\beta}$	Identified system damping coefficients [N.s/m] $\alpha,\beta=x,y$
$C_{SFD\alpha\beta}$	Identified squeeze film damping coefficients [N.s/m] $\alpha,\beta=x,y$
d	Orice diameter in flow restrictor [m]
D	$2R$. Damper journal diameter [m]
e	Amplitude or radius of circular centered orbit [m]
E_{dry}	Energy dissipated by dry-friction force [J]
E_{rv}	Energy dissipated by structure[J]
E_v	Energy dissipated by viscous forces [J]
$F_{x,y}$	External (shaker) forces applied to bearing [N]
$\overline{F}_x , \overline{F}_y$	Frequency components of external forces applied to bearing [N]
F_μ	Dry friction force from contact in mechanical seal [N]
f_n	Test system natural frequency [Hz]
$H_{\alpha\beta}$	Dynamic impedances [N/m], $\alpha,\beta=x,y$
K_{sx}, K_{sy}	Structural (support) stiffnesses [N/m]
L, R	Length and radius of SFD land [m]
M	Mass of bearing housing [kg]
M_f	Estimated mass of lubricant (feed plenum & end groove) [kg]
$M_{SFD\alpha\beta}$	Squeeze film inertia coefficients [kg], $\alpha,\beta=x,y$
$M_{s\text{-}\alpha\beta}$	Identified system inertia coefficients [kg], $\alpha,\beta=x,y$
P_a	Ambient pressure [bar]
P_s , P_r	Inlet (supply) pressure and pressure at recirculation annulus [bar]
Q	Lubricant flow rate [LPM]
T	Lubricant temperature [°C]
V	Velocity vector of bearing motions [m/s]
W	Work from external forces [J]
x,y	Bearing dynamic motions along X,Y directions [m]
$\overline{x}, \overline{y}$	Complex components of bearing motions [m]
$Z_{(\omega)}$	Vector of displacements in frequency domain [m]
ΔP_{SFDmax}	Max (P_s-P_r) [bar]
ΔP_{SFD}	P_s-P_r . Pressure difference across film land[bar]
ΔP_{ra}	P_s-P_a. Pressure difference across discharge flow restrictor [bar]
ϕ	Phase lag of damper motion relative to excitation force
μ	Dry friction coefficient from contact seal
ρ, η	Lubricant density [kg/m^3] and viscosity [Pa-s]
ω	Excitation frequency [rad/s]
ζ	$C/[2 (K_s M)^{1/2}]$. Viscous damping ratio

I Introduction

Squeeze film Dampers (SFDs) aid to reduce rotor vibrations and to increase stability margins in high performance rotating machinery. The forced performance (damping capability) of a SFD depends on its geometrical configuration and its operational parameters such as flow regime, type of journal motion, lubricant viscosity cavitation type, and air entrapment among others [1]. For numerous years, research efforts have been conducted to elucidate the parameters and configurations that maximize SFD performance for different applications.

Presently, with increasing rotor flexibilities and shaft speeds, high performance turbomachinery undergoes high dynamic loads and large displacements. Under these conditions, air ingestion and entrapment compromise the performance of SFDs with open ends or partially sealed configurations. Seal SFDs are essential for providing adequate damping under such demanding conditions, as they are less prone to air ingestion/entrapment than open end dampers when operating at high frequencies. Different types of seals have been adopted (O-rings, end plates, etc.), yet there are many more seals and other SFD geometric configurations (i.e. oil feeding arrangement, grooves) used in practice and not yet thoroughly investigated. A prior TRC technical report [2] presents a parameter identification for a contained SFD with a mechanical seal that effectively eliminates lubricant side leakage. This damper type, when not in use, must contain the lubricant in the film lands for extended periods of time. The test system force coefficients are identified from unidirectional dynamic loads. The test procedure first determines the system structural parameters as well as the equivalent viscous action of the dry-friction force at the mechanical seal interface. Next, squeeze film damping and inertia force coefficients are extracted from the test system force coefficients with lubricant flowing through the damper. This report furthers the experimental work advanced in [2], to asses the forced performance of the test damper under circular orbit motions.

II Literature Review

Della Pietra and Adilleta [3, 4] summarize most of the experimental and analytical works conducted on SFDs during the past 40 years. Reference [3] details the rudiments of SFD operation, the theoretical models advanced and the experimental research conducted on controlled motion test rigs. The topics reviewed include fluid inertia, groove geometry, end sealing, and lubricant cavitation and their effect on the forced performance of SFDs. Reference [4] addresses to rotordynamic analyses and field evaluation of SFDs installed in actual rotating equipment. The review closes with descriptions of unconventional and novel SFD designs.

References [5-10] report SFD parameter identification on controlled motion test rigs using time and frequency domain approaches. In general, where damping and inertia force coefficients have been experimentally determined, classical lubrication models render reliable predictions only for damping coefficients [11]. To date, the main issues of continued scrutiny include the proper prediction of fluid inertia coefficients, the adequate modeling of circumferential grooves and end seals, and the understanding of gas ingestion and entrapment.

Common end seals in SFDs include O-rings, piston rings, and end plates (clearance gap). The design of end seals is highly empirical and requires of "leakage correction factors" that can only be extracted from careful experimentation [12]. Levesley and Holmes [13] find experimentally that piston-ring end seals lead to larger damping coefficients than when using end plate seals, for example. On the other hand, from rotordynamic tests, De Santiago and San Andrés [14] show that integral dampers sealed with simple end plates are effective in increasing the overall damping while reducing the lubricant trough flow. The experiments show that rotor synchronous response amplitudes while crossing two critical speeds are proportional to the mass imbalance displacement, thus evidencing the linearity of the integral SFD elements. In [14], predictions of damping coefficients are in good agreement with the test data.

More recently, Kim and Lee [15] present both an analysis and tests of a sealed SFD with a central feeding groove. Two types of seals are modeled, a single-stage and two-stage liquid seals. Predictions including the two-stage seal agree with the test SFD inertia force coefficients, but underestimate the damping force coefficients.

For the past 20 years, the authors' research group has contributed to the extensive experimental and analytical body of work conducted on SFDs, including efforts to elucidate the issue of gas entrainment and entrapment; and advancing simple engineering models for reliable prediction of open-ends SFD forced performance, see [16, 17] for example. The research also focuses on the development of accurate parameter identification techniques with analysis of test data in the frequency domain [18]. In spite of the progress advanced, there are still issues to be fully understood. One is the poor correlation between predicted and experimentally derived added mass coefficients; with theory typically under predicting by ~50% the measurements. Another issue relates to end sealing, with some actual SFD configurations showing extreme complexity and few experimental results to verify their predicted performance. Thus, more analytical and experimental works are needed to fully understand and maximize the performance of SFDs.

This report extends prior art given in [2] by presenting dynamic load experiments generating circular centered orbits (CCO); a motion condition more realistic to the dynamics of rotating machinery. The aims are to extend the identification method to circular motions, to obtain the force coefficients of the SFD-seal system and SFD alone, and to assess any differences with earlier test results derived from unidirectional motions. Detailed descriptions of the test SFD rig, parameter identification procedure and experimental results follow.

III Test Rig Description

The test rig comprises of the same structure reported in a prior TRC research report [2]. Figure 1 depicts a schematic view of the test rig consisting of a bearing assembly and a vertical rigid shaft holding a steel journal, 127 mm (5") in diameter and 76.2 mm (3") in length. The shaft is supported on three precision ball bearings. The natural frequency of the shaft and journal equals 400 Hz [18]. The bearing assembly, shown in Figure 4, consists of an acrylic bearing sandwiched by two thick steel plates and connected with vertical steel plates. The composite bearing housing hangs from a top structure with four steel rods giving a structural stiffness to the test bearing section. On the top structure, a mechanism comprising of two flat plates - one able to slide- allows centering and off-centering positioning of the bearing with respect to its journal. The damper film land length *(L)* is 25.4 mm and the film radial clearance *(c)* is 127 μm ± 6 μm at room temperature (23 ^{0}C).
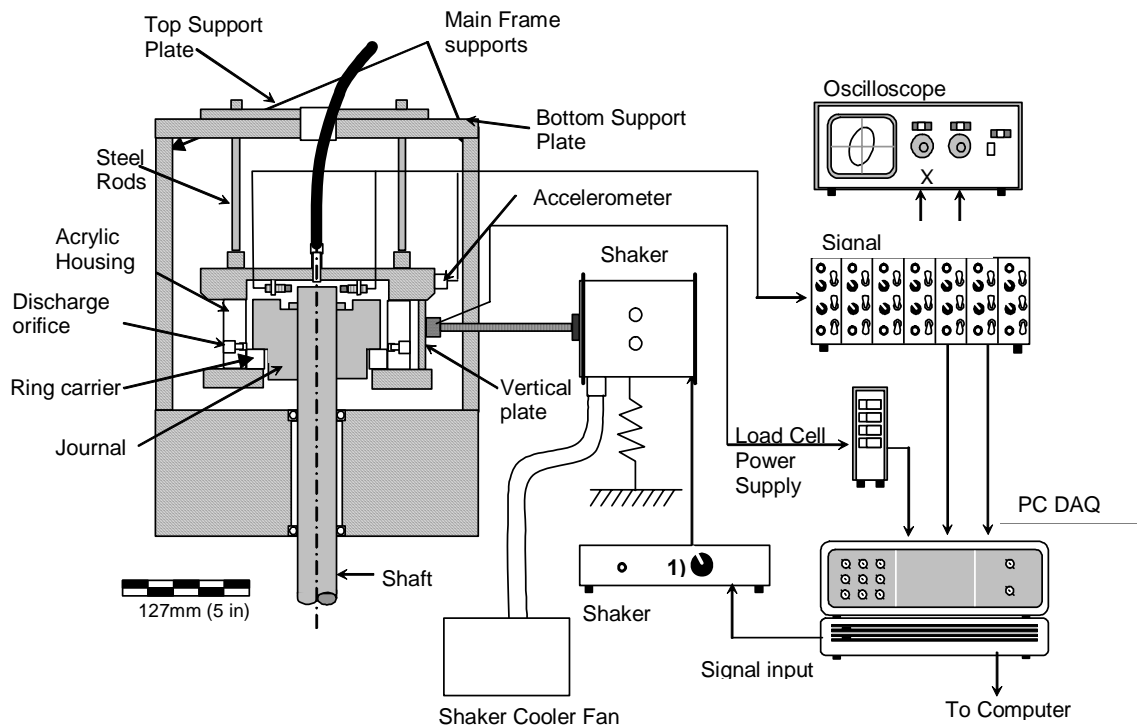
Figure 1 Test rig for dynamic force measurements and flow visualization in a sealed end SFD

Figures 2 and Figure 3 depict a cross section and a cut view of the end sealed SFD design along with its components, respectively. The bearing housing design integrates a SFD land and an annulus that accommodates a metallic ring (ring holder). This metallic ring along with the journal bottom surface provides a metal-metal mechanical seal. A wave spring, pushing the ring holder against the journal, applies a contact force between the matting surfaces. The bearing housing also incorporates a discharge recirculation annulus at one end of the squeeze film land, 4.25 mm deep and 7.62 mm in length. The oil is fed from the top and exits the damper at the recirculation annulus through four outlet ports. The discharge flow area is regulated by flow restrictors. The current tests include two sets of flow restrictors; one with 2.8 mm diameter holes, and other with 1.1 mm diameter holes.
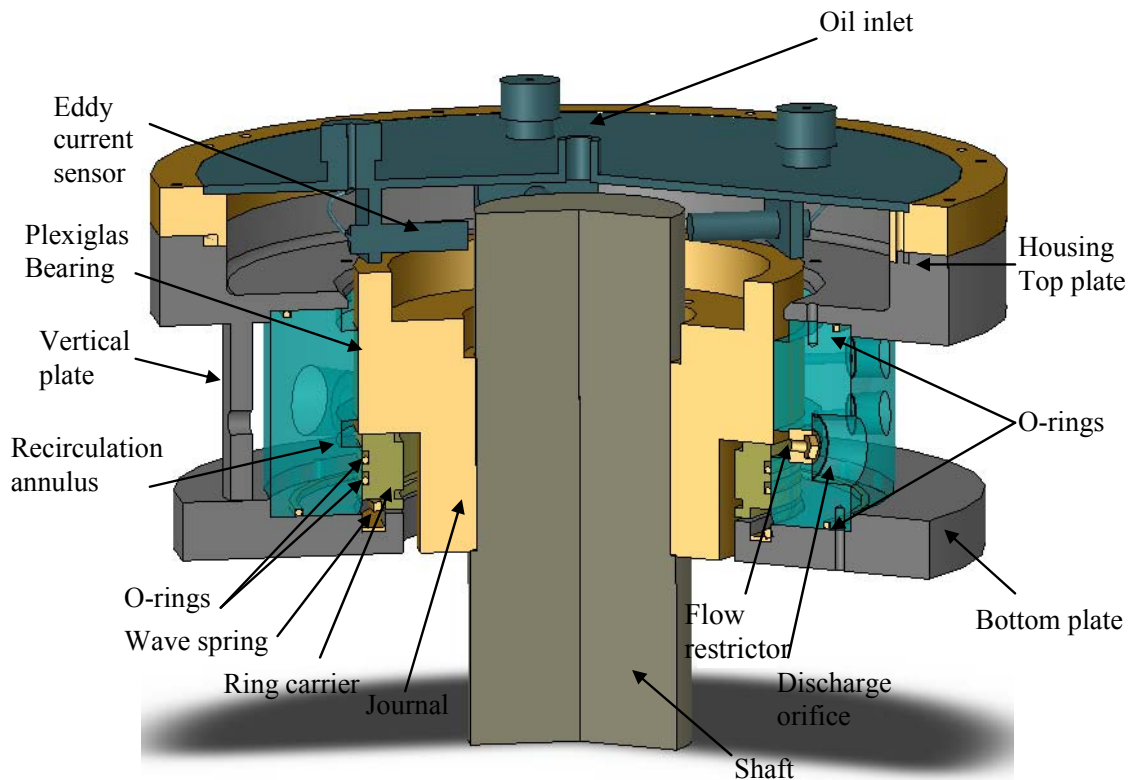
Figure 2 Sealed-end SFD assembly cross section view.
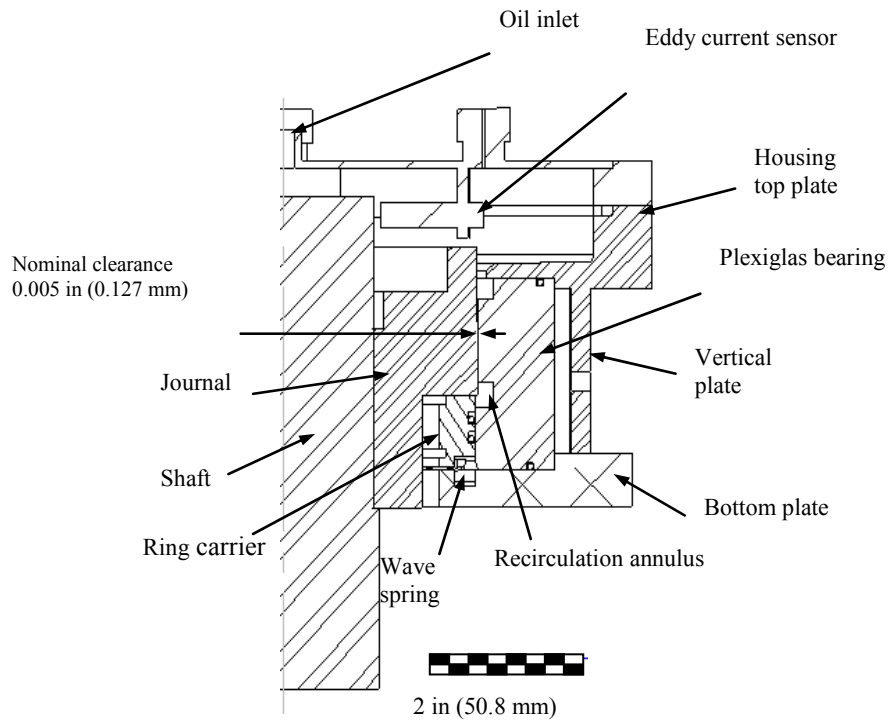
Figure 3 Sealed-end SFD assembly cut view.

Figure 4 shows the sensor disposition and reference coordinate system on the SFD housing. Two electromagnetic shakers (max. 100 lbf or 448 N), suspended from separate steel frames, stand to provide excitation forces onto the test device. Slender steel stingers connect the shaker to the bearing housing (*x* and *y* directions). Piezoelectric load cells are fastened to the side plates and the one of the stingers end. The top disk allocates two accelerometers *(x,y)*, right above the side plates.

1:Accelerometers
2: Load Cells
3: Stingers
4: Eddy current sensor holder
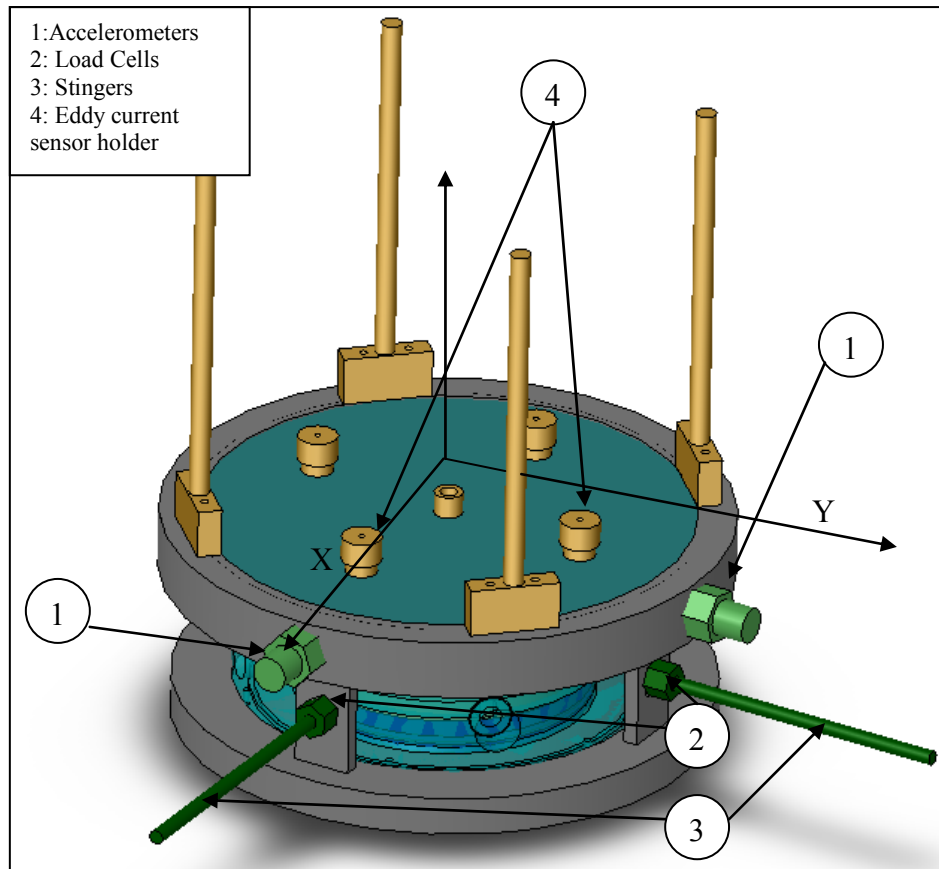
Figure 4 SFD housing reference coordinate system and location of sensors.

III.1 Data acquisition and post-processing

A DAQ board serves as an interface to connect the instrumentation, including pressure sensors, accelerometers, load cells and eddy current sensors to a PC. The data is recorded using a modified version of a Labview® virtual instrument (VI) initially designed by Diaz [19]. The modified version adds the following features:

* Control oil pump flow rate through motor frequency controller (using a relay box).

* Control magnitude and frequency of two shakers (real time-no need to stop operation)

* Control system to automatically adjust shaker input level to match a given load or displacement magnitude (selected by the user).

* Automated operation for multi-frequency tests.

A Mathcad® worksheet processes the recorded time traces (displacements, acceleration, forces), transform the data into the frequency domain, and perform the spectral analysis to obtain the test SFD force coefficients.

III.2 Lubrication system

Figure 5 depicts the lubrication system of the test rig, presently including two flowmeters and pipe lines for the four outlets of the new SFD configuration (end sealed). The flowmeters, located at the SFD inlet and outlet lubrication lines, allow estimation of leakage flow through the SFD end seal.
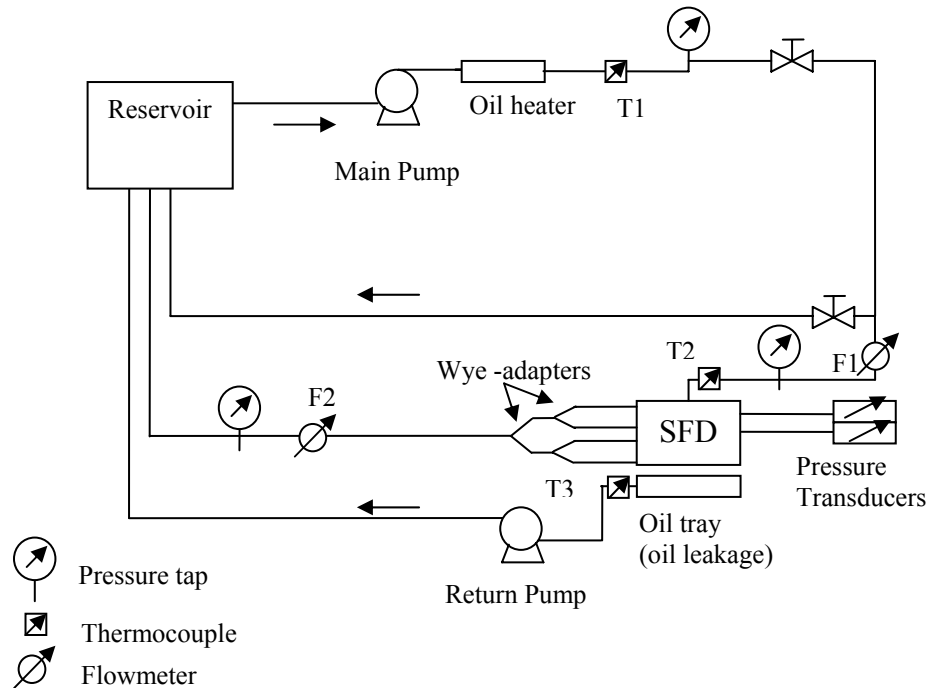
Figure 5 Schematic view of lubricant system.

The piping for connecting the SFD multiple oil outlets is symmetric in order to equalize the friction losses for each of the four outlets. This implies same longitude hoses and symmetric wye adapters.

The ISO VG 2 lubricant, specific gravity equal to 0.80, and its absolute viscosity depends on temperature (°C) as

$$\eta(T) = 2.8e^{-0.01665(T-23.6)} \text{ cPoise} \tag{1}$$

The relationship was obtained from viscosity measurements using a rheological viscometer [20].

IV Identification of Structural Parameters (Dry System)

A prior TRC report [2] notes that the main structure support with top plate (see Figure 1) has a natural frequency near the resonance frequency of the SFD assembly (i.e. 50 Hz), most notorious in the *X* direction. This indicates that the main structure is rather flexible and thus adds extra degrees of freedom to the test system. The best solution in this case is to restrict the motion of the main support and top plate, so the system can be properly modeled as a 2-DOF system. The natural frequency of the main structure increased to 150 Hz by stiffening the main supports that connect the top plate to the test rig base. This frequency is above the test rage (20 Hz-70 Hz). The modifications introduced required a re-estimation of the system structural parameters. Appendix A presents the identification of the structural system parameters (stiffness and mass), which follows a similar procedure as that in [2]. Table 1 shows the resulting mass and system stiffness.

Table 1 Structural stiffness coefficients and mass of bearing support

	K_{sx}[N/m]	K_{sy}[N/m]
Value	853 x10^3	885 x10^3
Uncertainty	34 x10^3 [~4%]	35 x10^3 [~4%]
Range[lb]	-25 to 25	-25 to 25
Mass	9.7 kg [±1%]	
f_n [Hz]	47±1	48±1

The estimation of the dry friction from periodic loads (circular orbits) follows.

IV.1 Periodic input load tests on "dry" system

Once the structural parameters are identified, the test system without any lubricant is exited with constant magnitude loads (44 N) from 20 Hz to 40 Hz using 2 Hz increments. The objective is to determine the dry friction force resulting from the interaction of the seal contact surfaces. The excitation loads exerted along both directions are 90^0 out of phase (i.e. circular load orbit). The chosen load amplitude is the minimum to induce motions of the system at 20 Hz.

Figure 6 depicts the fundamental frequency component of the ensuing bearin amplitudes along the *X* and *Y* directions. Note that the amplitudes of motion increase rapidly with frequency as the natural frequency is approached. Unlike in a prior TRC report [2], the current test frequency range excludes the natural frequency of the SFD

assembly (~ 48 Hz) since the vibrations of the dry system at 44 N reached the bearing clearance.
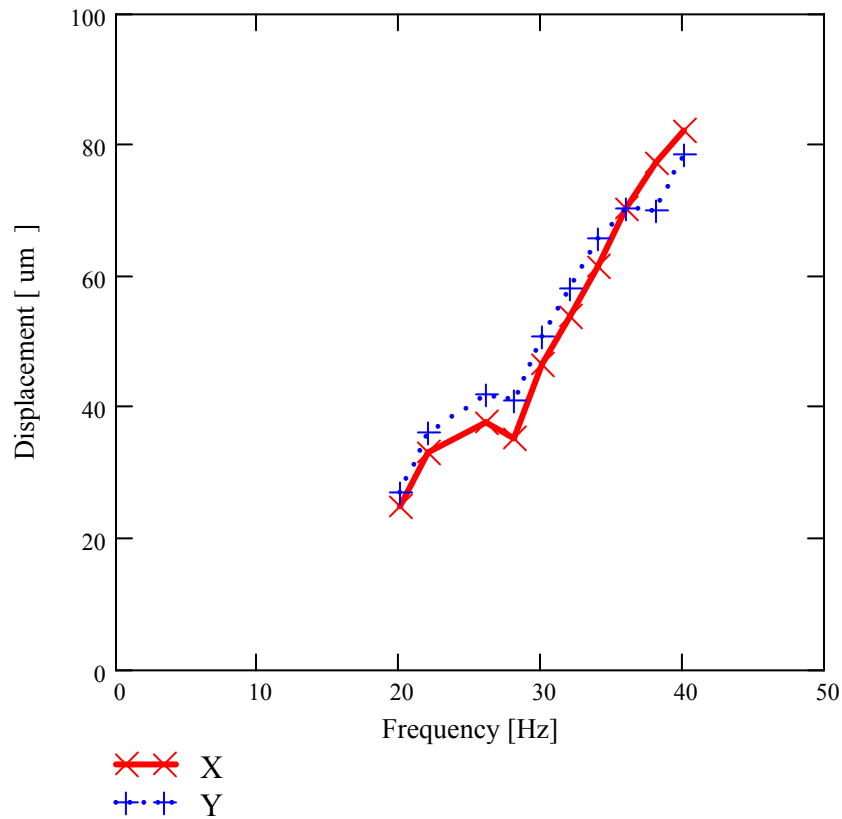
Figure 6 Amplitude of displacement response (fundamental frequency component) due to a constant magnitude circular orbit excitation (44 N). (Dry SFD, End seal in place)

IV.2 Identification of dry friction force from contacting seal ring

The equivalent damping coefficient with the mechanical seal in place (dry system) is obtained, as described in [2], by equating the work exerted by the external force to the energy dissipated by the system. The work exerted by the input external force is [21]

$$Work = \pi \left[|F_x||X|\sin(\phi_1) + |F_y||Y|\sin(\phi_2) \right] \qquad (2)$$

where (F_x, F_y) and (X, Y) are the force and response vectors; ϕ_1 and ϕ_2 are the phase lag of the response relative to the force along the X and Y directions, respectively. The energy dissipated by dry friction is [21]

18

$$E_{dry} = F_\mu \int_{t_1}^{t_1+T} |V| \, dt \tag{3}$$

where V is the velocity vector (V_x, V_y) constructed from the displacement Fourier coefficients (no velocity data is directly available). On the other hand, some energy is also dissipated by (residual) viscous effects

$$E_{rv} = C_{rv} \int_{t_1}^{t_1+T} \left(V_x^2 + V_y^2\right) dt \tag{4}$$

where C_{rv} is a residual viscous damping coefficient. The overall damping parameters are obtained assuming a combination of dry friction damping (arising from the end mechanical seal) and a residual viscous damping representing the small damping contribution from other sources (i.e. steel rods). The identification relies on equating $E_{dry} + E_{rv} = Work$.

The friction force relates to the magnitude of the contact force at the mechanical seal interface. Thus, the friction force can be modified by changing the compression of the wave spring that pushes ring holder against the journal bottom surface. The current contact force (i.e. normal force) at the seal interface is estimated at 90 N ($\pm$ 10 N) using the friction coefficient of the seal mating surfaces (μ ~0.37) identified in [2].

The magnitude of the residual viscous damping coefficient (C_{rv}= 60 Ns/m) is similar (within ~10 %) to the one obtained from impact tests on the dry system without the seal in place). This coefficient represents the viscous damping introduced by the support rods.

Figure 7 shows the work exerted by the input force and the estimated energy dissipated by the combined damping model for each test. The dissipated energy estimated with a friction force of 34 N and the remnant viscous damping 60 Ns/m, is in good agreement with the actual work input to the system.
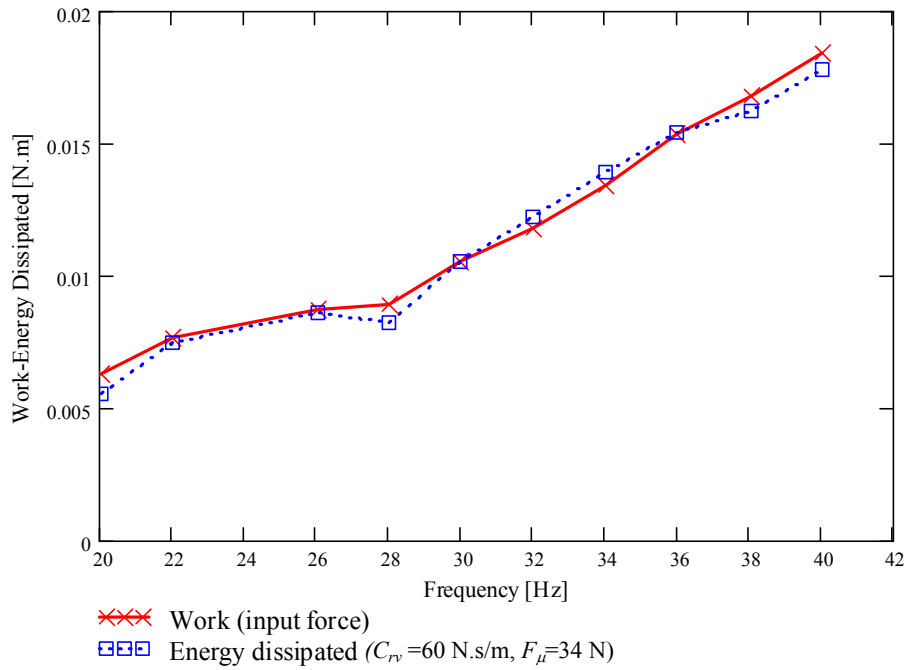
Figure 7 Work exerted by input force (= dissipated energy) estimated from combined damping model (Test 1). (Dry SFD, end seal in place)

Figure 8 depicts the ratio Im(F/X), which is proportional to the equivalent viscous damping coefficient for the dry system, i.e. $C\omega$. Notice that the viscous damping contribution, C_{rv}= 60 N.s/m, is rather small compared to the total viscous damping of the system. This indicates that the damping arising from the seal dry friction interaction (F_μ= 34 N) accounts for most of the system energy dissipation.
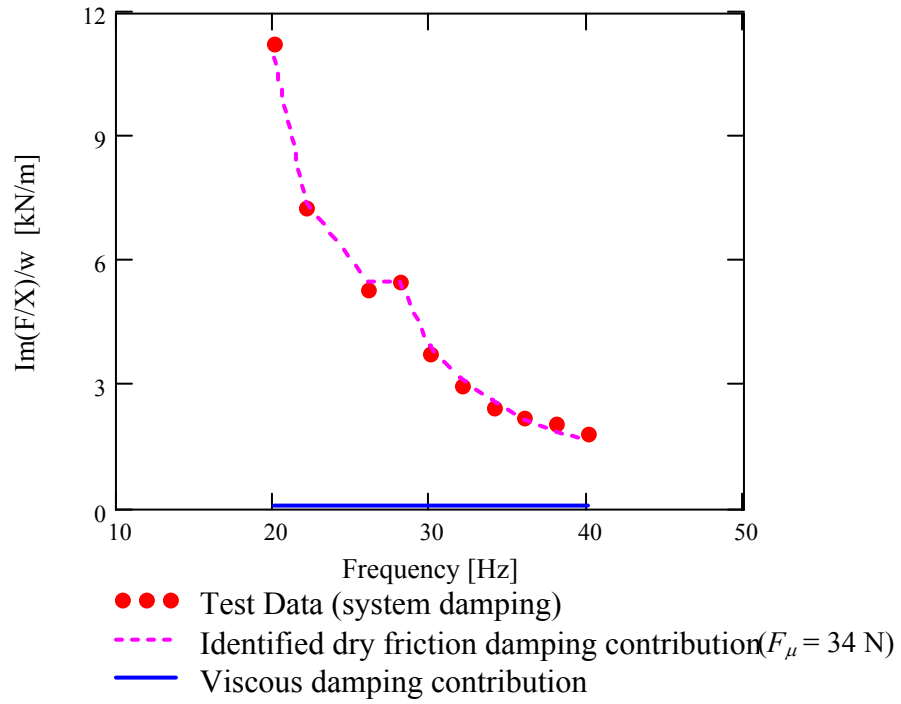
Figure 8 Equivalent viscous damping (dry friction + residual) versus excitation frequency. (Dry SFD, end seal in place)

V Measurements of flow rate in lubricated SFD

This section includes flow measurements using 1.1 mm diameter flow restrictors. Prior measurements in [2] were conducted with 2.8 mm diameter flow restrictors. Each flow restrictor consists of a pipe insert with a thru hole that restricts the outlet flow from the recirculation annulus. Figure 9 depicts a cross sectional area of the test system and featuring details of the flow restrictor.
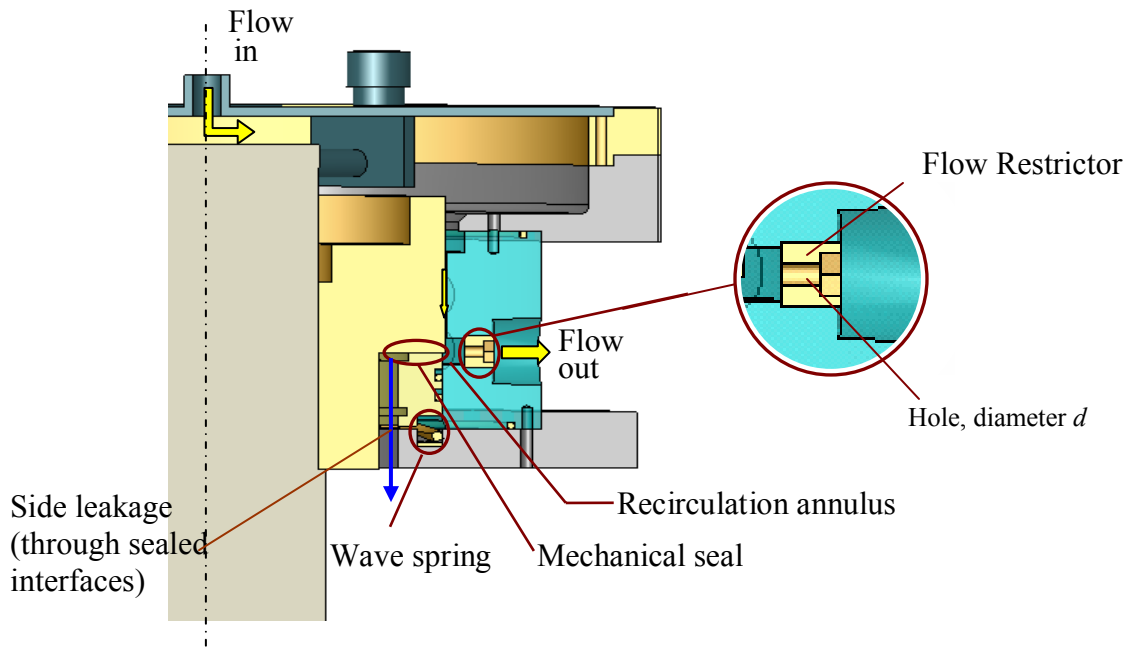
Figure 9 Cut view of SFD depicting a flow restrictor

The seal performance is determined by verifying that the mechanical seal assembly prevents side leakage of lubricant, and thus the recirculation annulus is completely filled with oil at all times. During the flow measurements, the seal effectively prevented any side leakage, thus indicating the contact force is sufficiently large to seal the interface between the damper journal and contact ring.

Figure 10 depicts the lubricant flow rate versus pressure drop across squeeze film land ($\Delta P_{SFD} = P_s - P_r$) for flow restrictors with holes of diameter 2.8 mm [2] and 1.1 mm. The graphs include results for three oil inlet temperatures (21-32 ^{o}C). Filled symbols represent the results for the restrictor with a hole of 2.8 mm. The measurements show that, as the oil temperature increases (viscosity decreases), the flow rate increases relative to the pressure differential across the damper film land. As expected, the lubricant flow

rates are similar for identical pressure differentials. Note that smaller size holes restrict the flow and increase the pressure in the recirculation annulus; thus then the smaller flow rates and pressure differentials recorded for 1.1 mm holes.
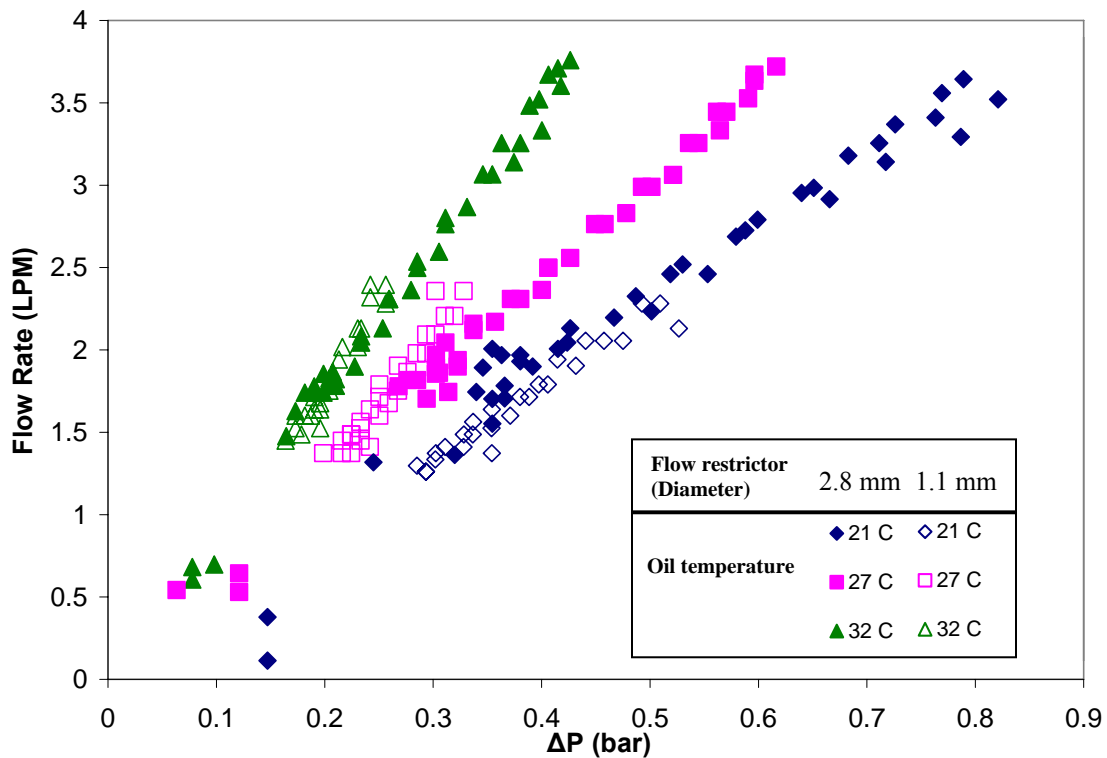
Figure 10 Lubricant flow rate through SFD vs. film land pressure differential $(P_s\text{-}P_r)$ (2.8 mm and 1.1 mm diameter flow restrictors)

Figure 11 presents the lubricant flow rate versus pressure drop across the flow restrictors, $\Delta P_{ra} = P_r\text{-}P_a$, when using 2.8 mm and 1.1 mm hole diameters. The pressure build up in the recirculation annulus with the small 1.1 mm diameter holes is about six times larger than for the larger orifices (2.8 mm); and consequently the lubricant flow rate is much lower (~ 50%) . Note that the relationship between flow rate and pressure differential is non linear.
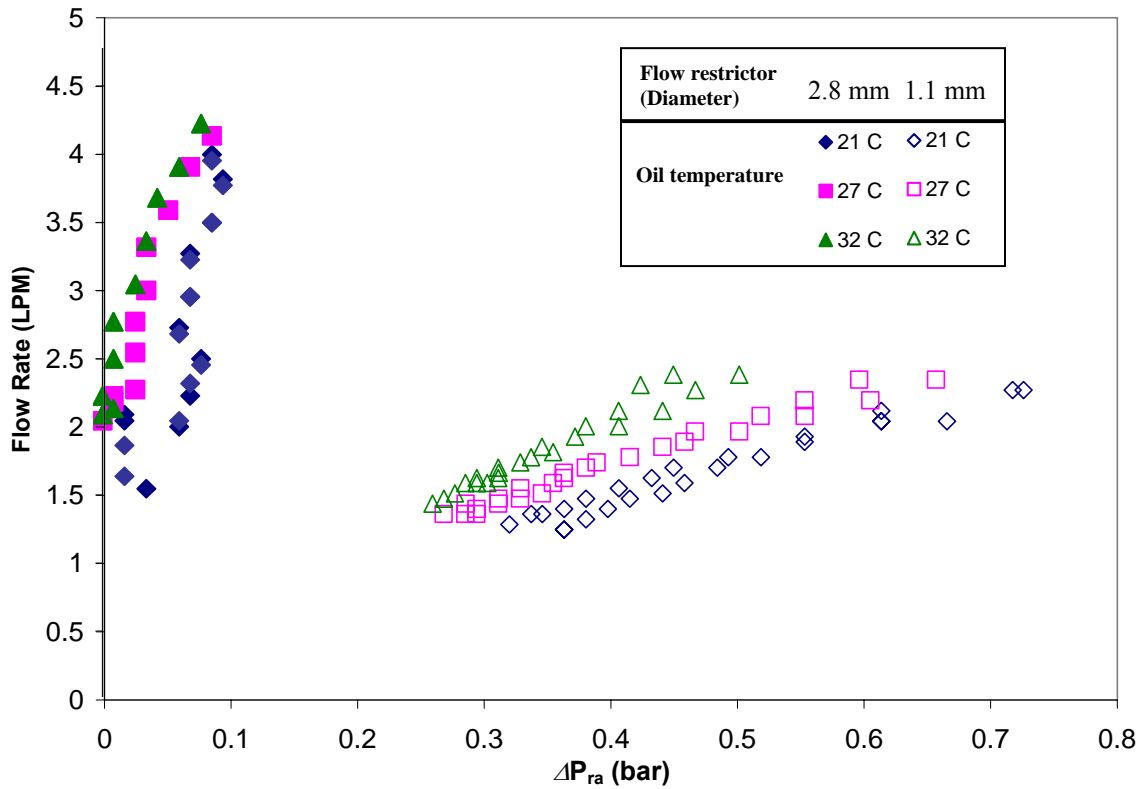
Figure 11 Lubricant flow rate versus pressure differential $\Delta P_{ra}= (P_r-P_a)$ across flow restrictor. Orifices of diameter 2.8 mm and 1.1 mm

Figure 12 depicts the pressure drop across the squeeze film land ($\Delta P=P_s-P_r$) versus the supply pressure for both sets of flow restrictors. The pressure drop across the damper land is smallest for the tightest restrictor, with a large build up of pressure at the recirculation annulus, as large as 0.7 bar. On the other hand, for the 2.8 mm diameter orifices, the pressure at the recirculation annulus is closer to ambient pressure (max $P_r\sim$ 0.12 bar). The pressure drop within the squeeze film land is proportional to the supply pressure, as expected.
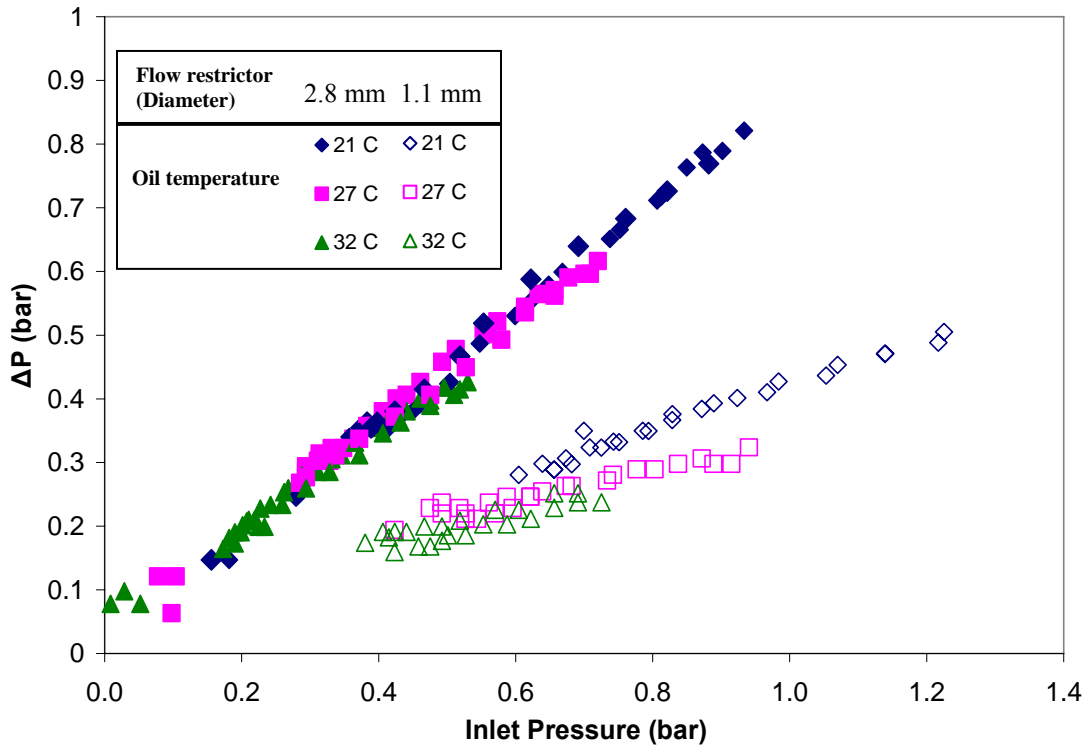
Figure 12 Pressure differential (ΔP=P$_s$-P$_r$) across squeeze film land versus supply pressure (2.8 mm and 1.1 mm diameter flow restrictors)

The analytical expression of the flow through the damper (centered journal) is [22]

$$Q = \frac{\pi D c^3}{12 \eta_{(T)}} \frac{P_s - P_r}{L} \tag{5}$$

where (c, D, L) are the damper radial clearance, diameter and length, respectively; (P_s-P_r) = ΔP_{SFD} is the pressure drop across the film land; and η is the lubricant viscosity, a function of the mean film temperature (T).

For both orifice diameters, Figure 13 shows the ratio recorded flow rate divided by predicted flow rate, Eq. (5), versus the film land pressure difference ratio $\Delta P_{SFD}/\Delta P_{max}$. The test flow ratio is ~ 1 (within a 20% band) for $\Delta P_{SFD}/\Delta P_{max} > 0.4$. Discrepancies, i.e ratios different than one, denote the need to reliably determine the operating clearance and oil temperature. Note that for low film land pressure differences, the flow rate is too small for the instruments to make an accurate measurement. As expected, the correlation is similar for both sets of flow restrictors.
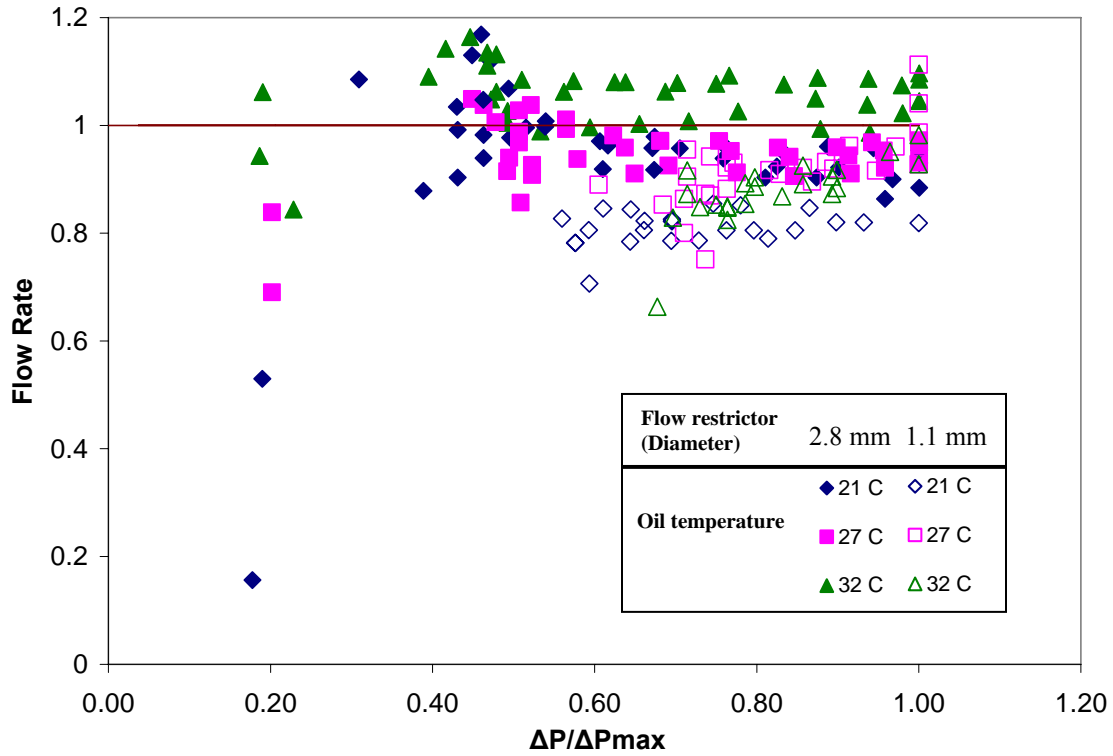
Figure 13 Ratio of test flow rate to predicted flow rate versus film land pressure difference ratio (2.8 mm and 1.1 mm diameter flow restrictors)

For later modeling of the sealed SFD, it is necessary to establish a relationship between the flow rate, the orifice diameter (d) and pressure drop $\Delta P_{ra}=P_r-P_a$ [23]

$$Q=4C_d \frac{\pi d^2}{4} \sqrt{\frac{2(P_r - P_a)}{\rho}} \tag{6}$$

where C_d is an empirical orifice coefficient. Figure 14 shows the ratio of the measured flow to the predictions derived from Eq. (6) versus the pressure differential ratio ($\Delta P_{ra}/max(\Delta P_{ra})$) for the 1.1 mm diameter restrictor. The results show a ratio nearly equal to one, thus demonstrating Eq. (6) models best the flow through the orifice. For the predictions, an orifice discharge coefficient $C_d=1$ was used.

For the largest orifice (2.8 mm), the pressure at the recirculation annulus is nearly ambient pressure, thus the flow rate is largest and not regulated by the orifice restrictor.

Further analysis will be conducted later to find the equivalent flow resistance of the test system, i.e. squeeze film land and orifices in series, to determine an "end seal" like coefficient for usage in predictions of SFD forced performance.
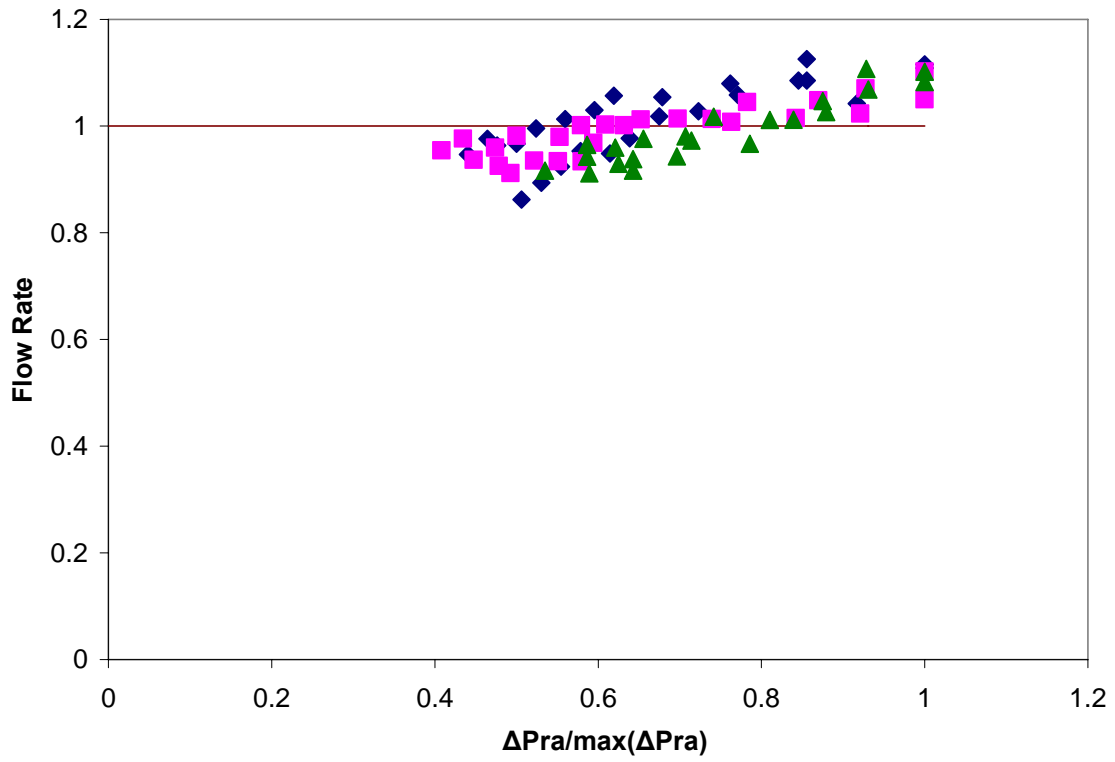
Figure 14 Ratio of test flow rate to predicted flow rate versus recirculation annulus pressure difference ratio (1.1 mm diameter flow restrictor)

VI Identification of Squeeze Film Damping and Inertia Coefficients for Lubricated SFD

VI.1 Experimental procedure

With lubricant flowing through the damper lands, single frequency dynamic loads are applied into the test system to produce centered circular orbits (CCO). The tests include four increasing motion amplitudes (12 μm to 50 μm) at frequencies ranging from 20 Hz to 70 Hz. and for two sets of flow restrictors (2.8 mm and 1.1mm diameter holes). The largest motion amplitude amounts to ~ 40% of the damper radial clearance. Table 1 presents the test conditions.

Table 2 Test conditions for dynamic load tests (CCO). Lubricated SFD

Inlet Pressure (P_s)[*]	31 kPa
Recirculation Annulus Pressure (P_r)*	8.6 kPa-15.5 kPa
Frequency Range	20-70 Hz (2 Hz step)
Lubricant temperature (T)	23-25 ^{0}C (73-77 ^{0}F)
Viscosity (η)	3.1 cP- 2.8 cP
Clearance (c)	125-127 μm (4.9-5 mils)
Orbit amplitude (e)	12-50 μm (0.5-2 mils)
Flow restrictors (hole diameter)	2.8 mm and 1.1mm

*: Gauge pressure.

Throughout the test frequency range, the applied dynamic load is set to maintain constant amplitude circular orbits (12 μm, 25 μm, 38 μm, 50 μm). Figures 15 through 18 show the applied loads (*Y vs.* X) and ensuing displacement orbits at 20 Hz and 70 Hz for the two flow restrictor configurations tested. Appendix C includes excitation force and displacements orbits at other selected frequencies ranging from 20 Hz to 70 Hz.
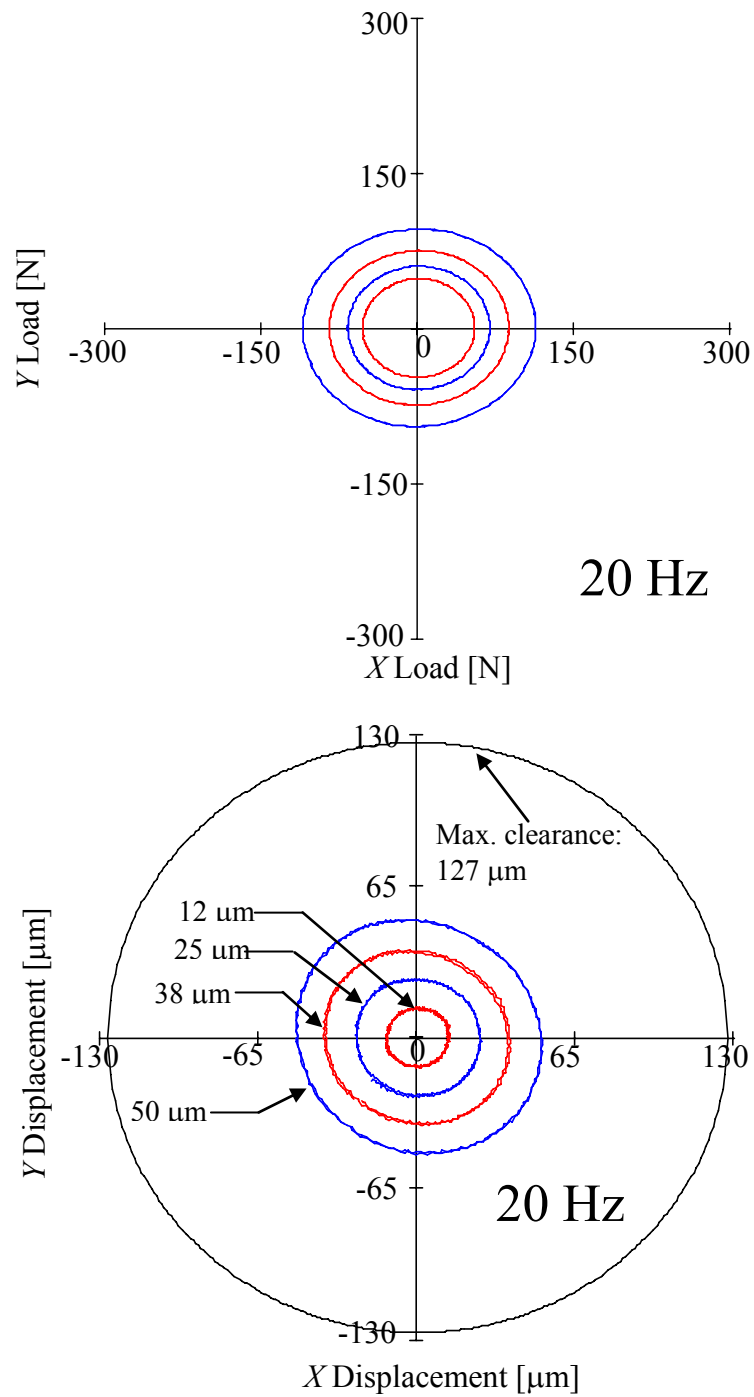
Figure 15 Recorded load and ensuing displacement orbits for four amplitude load levels. Clearance circle noted . (20 Hz, lubricated SFD, CCO, 2.8 mm diameter flow restrictor)
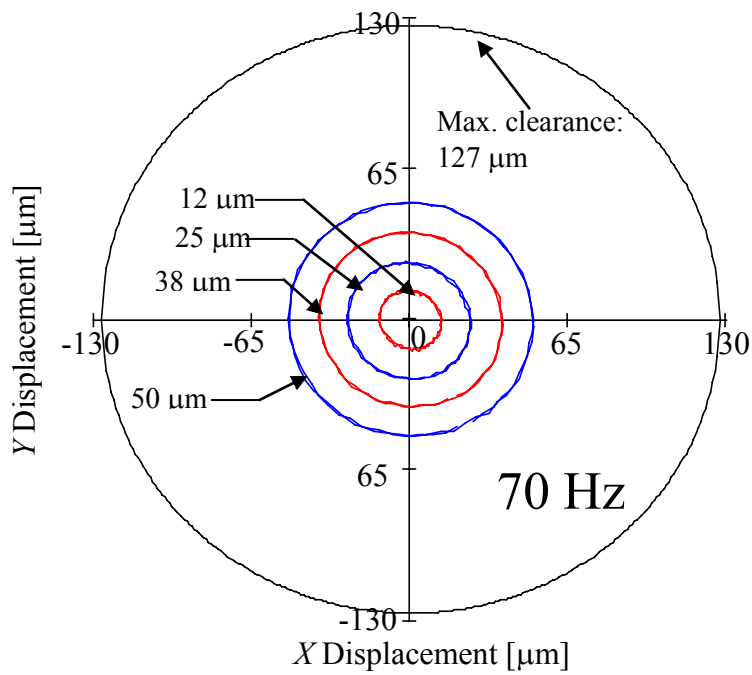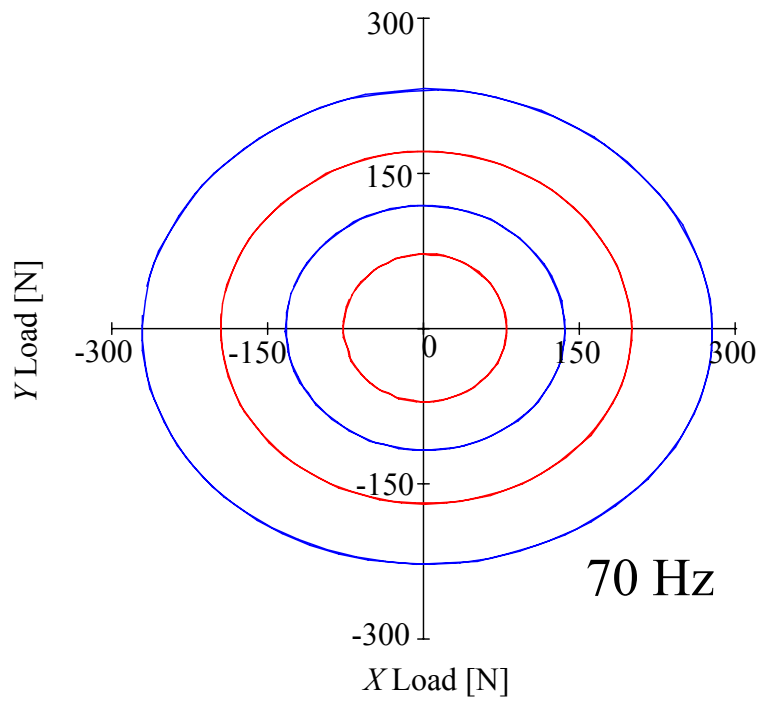
Figure 16 Recorded load and ensuing displacement orbits for four amplitude load levels. Clearance circle noted. (70 Hz, lubricated SFD, CCO, 2.8 mm diameter flow restrictor)
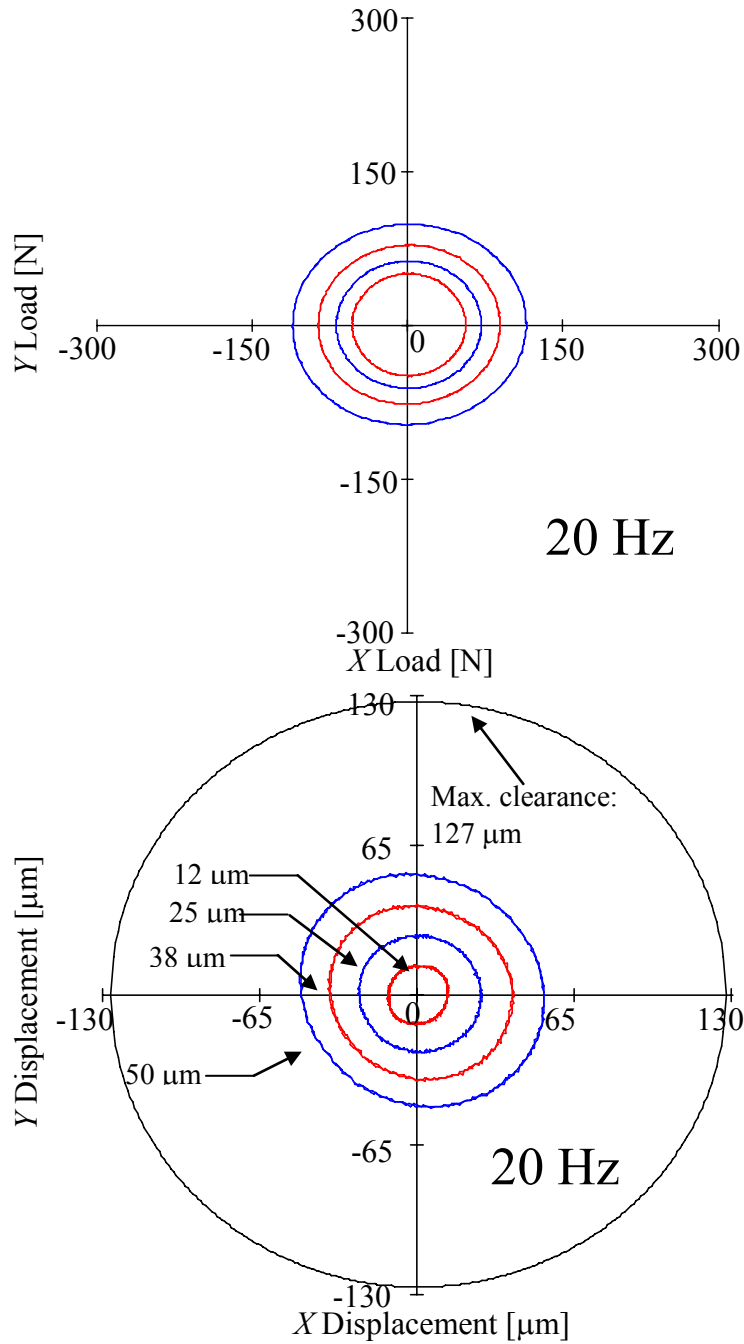
Figure 17 Recorded load and ensuing displacement orbits for four amplitude load levels. Clearance circle noted. (20 Hz, lubricated SFD, CCO, 1.1 mm diameter flow restrictor)
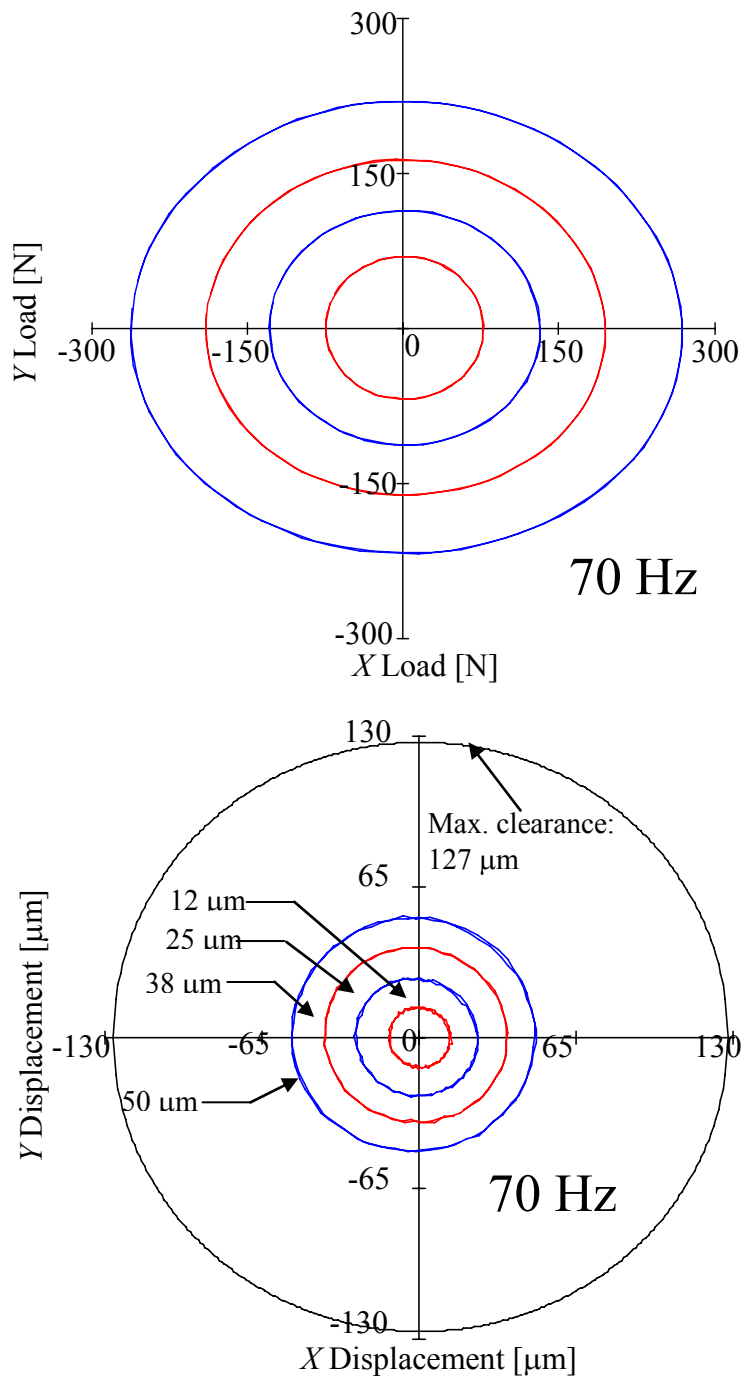
Figure 18 Recorded loads and ensuing displacement orbits for four amplitude load levels. Clearance circle noted. (70 Hz, lubricated SFD, CCO, 1.1 mm diameter flow restrictor)

Figures 19 and 20 show the amplitude of the dynamic load versus frequency when using 2.8 mm and 1.1 mm diameter flow restrictors, respectively. The dynamic load increases steadily with frequency in order to maintain the design (preset) constant orbit amplitude. The amplitudes of bearing orbital motion are labeled on each graph.
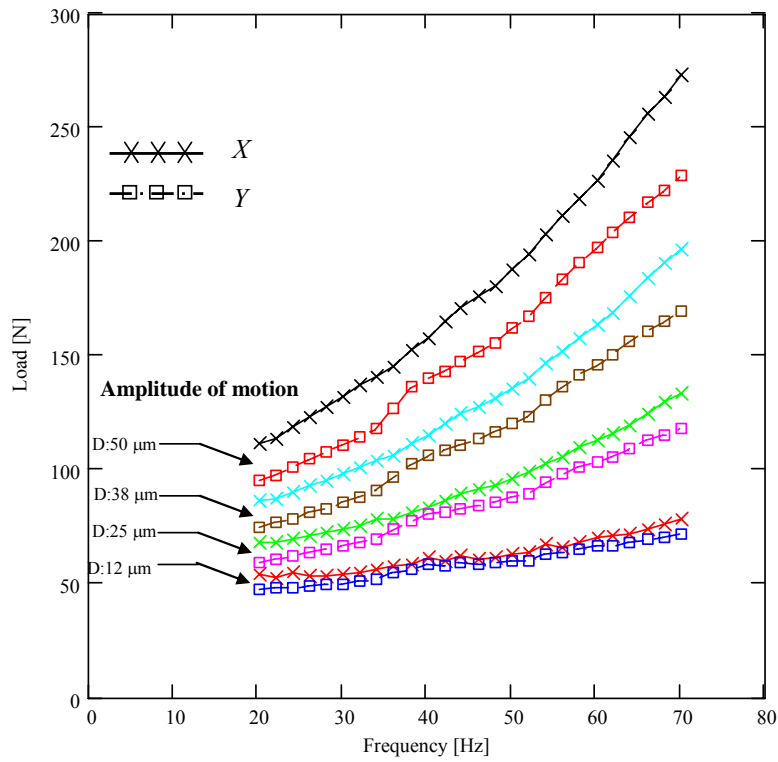
Figure 19 Amplitudes of dynamic load versus excitation frequency (4 tests- CCO, lubricated SFD, 2.8 mm diameter flow restrictor)
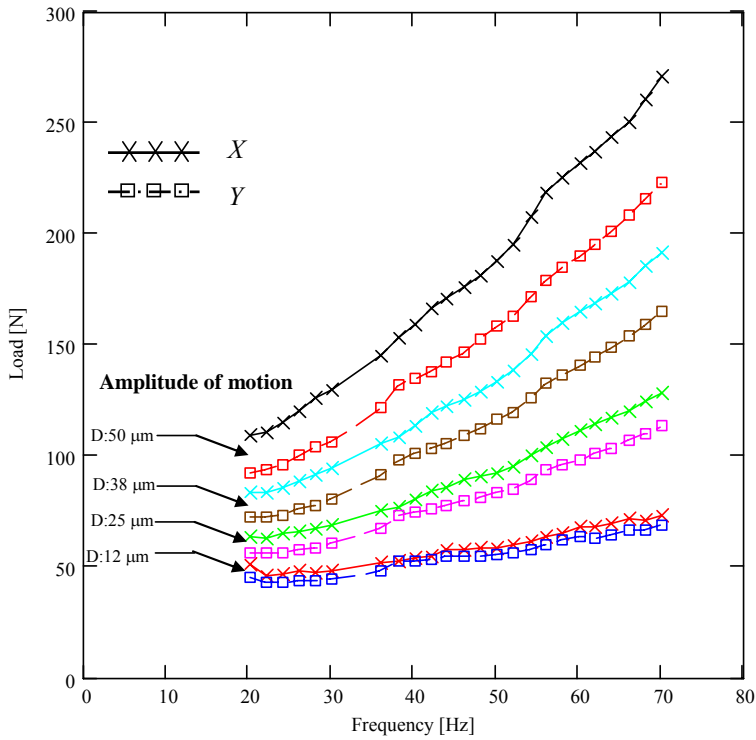
Figure 20 Amplitudes of dynamic load versus excitation frequency (4 tests- CCO, lubricated SFD, 1.1 mm diameter flow restrictor)

Figures 21 and 22 depict the hydrodynamic pressure waves at the SFD land and recirculation annulus when exiting the system at 70 Hz, for the two sets of flow restrictors used. In the case of the configuration with the larger flow area (2.8 mm holes) the dynamic pressure in the SFD land reaches lower values than that recorded when using the smaller flow restrictor configuration. For both flow restrictor configurations, there are no signs of oil cavitation or air entrapment, thus evidencing the effectiveness of the mechanical seal. Regarding the pressure at the recirculation annulus, the configuration with 2.8 mm diameter holes shows larger dynamic pressures than those obtained when using 1.1 mm diameter flow restrictors; however the static (mean) pressure is lower. This difference is attributed to a variation of the sensor gain as explained below.
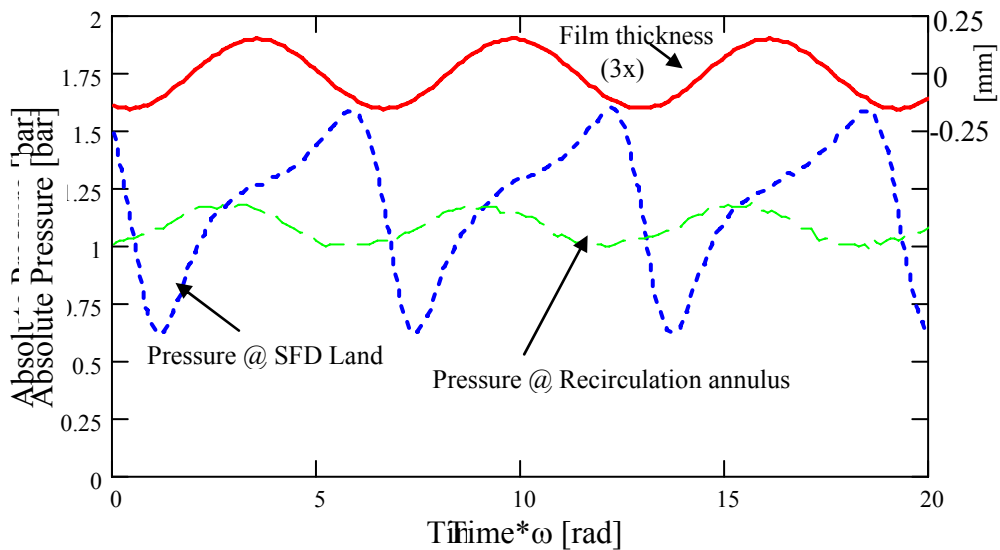
Figure 21 Dynamic pressure measurements at SFD land and recirculation annulus (including film thickness at sensor location). (70 Hz, 50 μm orbit amplitude, 2.8 mm flow restrictor, supply Pressure= 31 kPa)-Film thickness amplified (3x) to enhance view.

Figure 22 Dynamic ressure measurements at SFD land and recirculation annulus (including film thickess at sensor location). (70 Hz, 50 μm orbit amplitude, 1.1 mm flow restrictor, supply Pressure= 31 kPa)-Film thickness amplified (3x) to enhance view.

Figure 23 shows the peak to peak values of the dynamic pressure waves recorded at the SFD land and recirculation annulus for each set of flow restrictors (2.8 mm and 1.1 mm diameter flow restrictors) for 50 μm orbit amplitudes. Figure 24 presents similar results recorded for 12 μm orbit amplitudes. Note the difference of scales between Figures 23 and 24. For both sets of flow restrictors the peak pressures show the same trend. The dynamic pressures in the SFD land for the largest amplitude (50 μm) are considerably larger than those recorded for the small orbit of 12 μm. Furthermore, the pressure at the SFD land for the 12 μm amplitude orbits is similar to the pressure recorded at the recirculation annulus for the same orbit amplitude.

On the other hand, the pressure at the recirculation annulus for both sets of flow restrictors is nearly independent of the frequency and similar for both sets up to 40 Hz. From 40 Hz the recirculation annulus pressure fluctuation for the larger flow restrictor increases and deviates from the value for the smaller flow restrictor. The rationale for the sudden increase is most likely due to a change in the flow field within the recirculation annulus.

Note that for the 2.8 mm diameter flow restrictors and at the highest test frequencies, the gradient of the pressure in the SFD land is slightly larger than that recorded when

35

using 1.1 mm flow restrictors. This indicates that the latter configuration is slightly less prone to oil cavitation than the other configuration (2.8 mm).
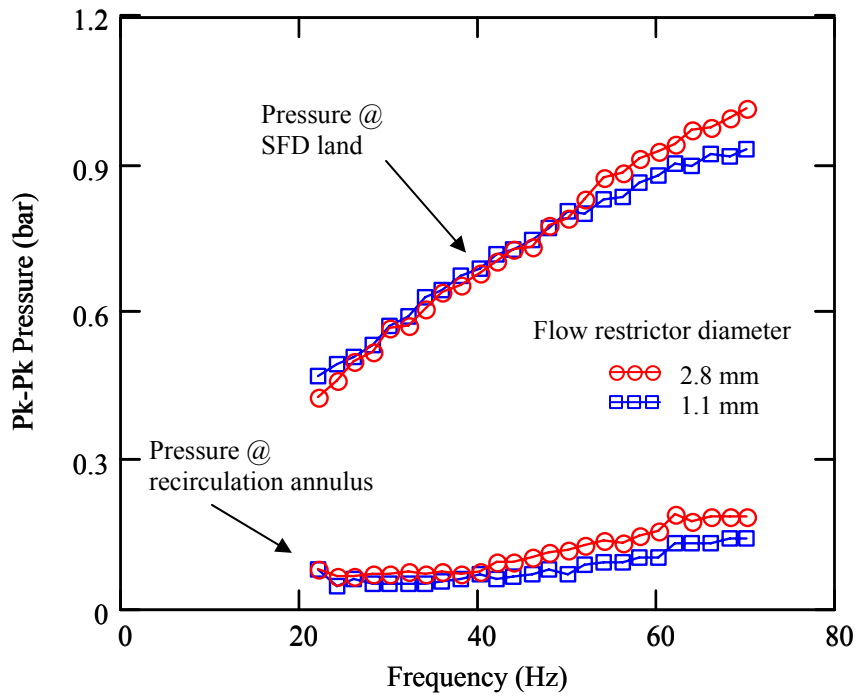
Figure 23 Pk-pk dynamic pressures in SFD land and recirculation annulus. (50 μm orbit amplitude, 2.8 mm and 1.1 mm diameter flow restrictor)
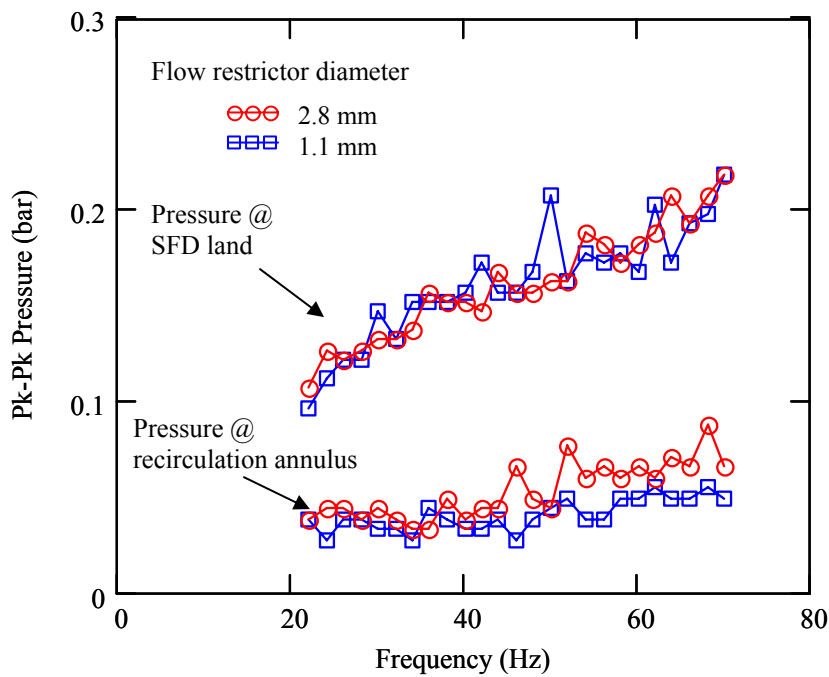
Figure 24 Pk-pk dynamic pressures in SFD land and recirculation annulus. (12 μm orbit amplitude, 2.8 mm and 1.1 mm diameter flow restrictor)

VI.2 Parameter identification method

This section describes the identification method employed to estimate the SFD parameters from centered circular orbit tests. The equations of motion for the test bearing section are

$$\begin{bmatrix} M+M_f & 0 \\ 0 & M+M_f \end{bmatrix}\begin{Bmatrix} \ddot{x} \\ \ddot{y} \end{Bmatrix} + \begin{bmatrix} K_{sx} & 0 \\ 0 & K_{sy} \end{bmatrix}\begin{Bmatrix} x \\ y \end{Bmatrix} = \begin{Bmatrix} F_x \\ F_y \end{Bmatrix} - \begin{Bmatrix} F_x \\ F_y \end{Bmatrix}_{seal} - \begin{Bmatrix} F_x \\ F_y \end{Bmatrix}_{SFD} \tag{7}$$

where M_f =0.62 kg represents the estimated mass of fluid enclosed in the plenum above the fluid film land section and in the recirculation annulus. The SFD reaction forces follow the linearized description:

$$\begin{Bmatrix} F_x \\ F_y \end{Bmatrix}_{SFD} = \begin{bmatrix} C_{SFD\,xx} & C_{SFD\,xy} \\ C_{SFD\,yx} & C_{SFD\,yy} \end{bmatrix}\begin{Bmatrix} \dot{x} \\ \dot{y} \end{Bmatrix} + \begin{bmatrix} M_{SFD\,xx} & M_{SFD\,xy} \\ M_{SFD\,yx} & M_{SFD\,yy} \end{bmatrix}\begin{Bmatrix} \ddot{x} \\ \ddot{y} \end{Bmatrix} \tag{8}$$

where $\{C_{SFD_{\alpha\beta}}\}_{\alpha\beta=x,y}$, $\{M_{SFD_{\alpha\beta}}\}_{\alpha\beta=x,y}$ are the squeeze film damping and inertia force coefficients, respectively. The mechanical seal reaction force is expressed as

$$\begin{Bmatrix} F_x \\ F_y \end{Bmatrix}_{seal} = F_\mu \begin{Bmatrix} \dfrac{\dot{x}}{|V|} \\ \dfrac{\dot{y}}{|V|} \end{Bmatrix} \approx \begin{Bmatrix} C_{seal_x}\dot{x} \\ C_{seal_y}\dot{y} \end{Bmatrix} \tag{9}$$

where $V=(\dot{x},\dot{y})^{\mathrm{T}}$ is the velocity vector *and* F_μ is the dry-friction force and. C_{seal} is an equivalent viscous damping coefficient that follows from equating the energy dissipated by viscous forces to the energy dissipated from dry friction forces over one period of motion [20],

$$C_{seal}\oint|V|^2 dt = E_{dry} = F_\mu \oint V sign(V)dt \rightarrow C_{seal} = \frac{F_\mu}{\omega|x_\alpha|}; \alpha=x,y \tag{10}$$

In the frequency domain the system can be represented as

$$\left[-\omega^2 \boldsymbol{M} + i\omega \boldsymbol{C} + \boldsymbol{K} \right] Z_{(\omega)} = \underline{H}_{(\omega)} Z_{(\omega)} = F_{(\omega)} \tag{11}$$

where

$$\mathbf{M} = \begin{bmatrix} M_{s-xx} & M_{s-xy} \\ M_{s-yx} & M_{s-yy} \end{bmatrix}, \quad \boldsymbol{K} = \begin{bmatrix} K_{s_x} & 0 \\ 0 & K_{s_y} \end{bmatrix}, \quad \boldsymbol{C} = \begin{bmatrix} C_{s-xx} & C_{s-xy} \\ C_{s-yx} & C_{s-yy} \end{bmatrix};$$

with

$$C_{s-xx} = C_{SFD_{xx}} + C_{seal} + C_{rv}; \quad C_{s-yy} = C_{SFD_{yy}} + C_{seal} + C_{rv}; \tag{12}$$

$$C_{s-yx} = C_{SFD_{yx}}; \quad C_{s-xy} = C_{SFD_{xy}}$$

$$M_{s-xx} = M_{SFD_{xx}} + M_f + M; \quad M_{s-yy} = M_{SFD_{yy}} + M_f + M;$$

$$M_{s-yx} = M_{SFD_{yx}}; \quad M_{s-xy} = M_{SFD_{xy}}$$

and $Z_{(\omega)}, F_{(\omega)}$ are the discrete Fourier Transform (DFT) of time varying displacements and forces, respectively. In particular, a periodic forcing function can be represented as

$$F_x(t) = F_{xc}\cos(\omega t) + F_{xs}\sin(\omega t) = \left(F_{xc} - i F_{xs} \right) e^{i\omega t} = \overline{F}_x e^{i\omega t}$$

$$\tag{13}$$

$$F_y(t) = F_{yc}\cos(\omega t) + F_{ys}\sin(\omega t) = \left(F_{yc} - i F_{ys} \right) e^{i\omega t} = \overline{F}_y e^{i\omega t}$$

Subsequently, the bearing displacement and accelerations are also periodic with identical frequency (ω), and expressed as

$$Z_{(\omega)} = \begin{Bmatrix} x \\ y \end{Bmatrix} = \begin{Bmatrix} x_c - i x_s \\ y_c - i y_s \end{Bmatrix} e^{i\omega t} = \begin{Bmatrix} \overline{x} \\ \overline{y} \end{Bmatrix} e^{i\omega t}; \quad \begin{Bmatrix} \ddot{x} \\ \ddot{y} \end{Bmatrix} = \begin{Bmatrix} \overline{a}_x \\ \overline{a}_y \end{Bmatrix} e^{i\omega t} \tag{14}$$

For circular motions, the displacements along x and y are of identical magnitude but 180^0 out of phase, $\overline{y} = -i\overline{x}$. Then, Eq. (7) becomes

$$\left(K_{s_x} - \omega^2 M_{s-xx} + \omega C_{s-xy} \right) + i\left(\omega C_{s-xx} + \omega^2 M_{s-xy} \right) = \left(\frac{\overline{F}_x}{\overline{x}} \right)$$

$$\tag{15}$$

$$\left(K_{s_y} - \omega^2 M_{s-yy} + \omega C_{s-yx} \right) + i\left(\omega C_{s-yy} + \omega^2 M_{s-yx} \right) = \left(\frac{\overline{F}_y}{\overline{y}} \right)$$

where $M_{s\text{-}xx}$, $C_{s\text{-}xx}$, $M_{s\text{-}yy}$ and $C_{s\text{-}yy}$ represent the <u>test system</u> inertia and damping force coefficients, see elements in matrices of Eq. (12). The system mass coefficients can be readily identified from Eq. (15). The real part of the complex dynamic stiffness $\left(\left(\dfrac{\overline{F}_x}{x} \right), \left(\dfrac{\overline{F}_y}{y} \right) \right)$ is curve fitted to a second order polynomial (with $C_{s\text{-}xy} = C_{s\text{-}xy} = 0$), rendering correlation values of 97 %. The inertia of the squeeze film is extracted from the expression:

$$M_{SFDxx} = M_{s-xx} - M - M_f$$
$$M_{SFDyy} = M_{s-yy} - M - M_f \tag{16}$$

The <u>system</u> damping coefficients are obtained from the imaginary part of the dynamic stiffnesses in Eq. (15), i.e.

$$C_{s-xx} = \frac{\mathrm{Im}\left(\dfrac{\overline{F}_x}{x} \right)}{\omega} \quad , \quad C_{s-yy} = \frac{\mathrm{Im}\left(\dfrac{\overline{F}_y}{y} \right)}{\omega} \tag{17}$$

where $M_{s\text{-}xy} = M_{s\text{-}yx} = 0$ since the squeeze film does not show any lubricant cavitation. Squeeze film coefficients at each excitation frequency follow from

$$C_{SFDxx} = C_{s-xx} - C_{seal} - C_{rv}$$
$$C_{SFDyy} = C_{s-yy} - C_{seal} - C_{rv} \tag{18}$$

where $C_{rv} = 60$ N.s/m and C_{seal} is given in Figure 7($F_\mu = 34$ N). This approach renders damping coefficients that vary with test frequency. A more suitable method, reducing uncertainty in the identification, substitutes $\omega C_{seal} = \dfrac{F_\mu}{|x|}$ into Eq. (17) to render

$$\omega\, C_{SFD_{xx}} = \mathrm{Im}\left(\frac{\overline{F}_x}{x} \right) - \frac{F_\mu}{|\overline{x}|} - \omega\, C_{rv}$$
$$\omega\, C_{SFD_{yy}} = \mathrm{Im}\left(\frac{\overline{F}_y}{y} \right) - \frac{F_\mu}{|\overline{y}|} - \omega\, C_{rv} \tag{19}$$

A first order curve fit of Eq. (19) over the test frequency range renders the squeeze film damping coefficients C_{SFDxx} and C_{SFDyy}. Note that these coefficients represent

"average" values over a frequency range. Appendix D presents the imaginary part of the dynamic impedances and the right hand side of Eq. (19) for all the load amplitudes tested. The data shown evidences the differences from both procedures, i.e. frequency average from linear curve fit and local slope of imaginary part of transfer function.

For comparison to the identified parameters, the direct damping coefficient for a short length open ends SFD describing circular centered orbits is [1]

$$\left(C_{SFDxx} = C_{SFDyy} \right)_{theory} = \frac{\pi \eta R}{\left(1 - \left[\dfrac{e}{c} \right]^2 \right)^{3/2}} \left(\frac{L}{c} \right)^3 \tag{20}$$

This formula applies to a full film. Above e is the orbit radius and η is the lubricant viscosity. At the temperature tested, the measured clearance *(c)* equals 0.125 mm. The predicted fluid inertia coefficient, Eq. (21) below, uses twice the physical length of the damper land when properly accounting for the outlet boundary condition in the test SFD element, [24]

$$\left(M_{SFDxx} = M_{SFDyy} \right)_{theory} = \frac{\rho \pi R (2L)^3}{2 \times 10 c} \tag{21}$$

VI.3 Results: Dynamic force coefficients for lubricated system

This section presents the SFD added mass and damping force coefficients identified from the circular centered orbit tests when using 2.8 mm and 1.1 mm diameter flow restrictors.

Figure 25 depicts the real part of the dynamic stiffnesses and the curve fits ($K_{s\text{-}\alpha\alpha}$ - $\omega^2 M_{s\text{-}\alpha\alpha}$, $\alpha=x,y$) that render the system inertia coefficients for the largest amplitude of motion (50 μm). Notice the substantial drop in the test system natural frequency, from 48 Hz to ~34 Hz, due to the large fluid inertia in the squeeze film land and recirculation groove.

Table 3 presents the structural parameters (see Appendix A) and the identified inertia coefficients for both sets of flow restrictors. The predicted film inertia coefficients are within ~16 % of the test identified inertia coefficients. Furthermore, the identified squeeze film inertia coefficient are similar (within 8%) to those obtained from unidirectional load tests in [2], i.e. M_{SFDxx}=9.4 kg and M_{SFDyy}=8.1 kg. The flow restrictor size does not affect the magnitude of the fluid inertia coefficient.

Table 3 SFD inertia coefficients identified from circular centered orbit tests (amplitude of motion: 50μm, frequency range 20-70 Hz)

Flow restrictor size	2.8 mm		1.1 mm	
Parameter	*xx*	*yy*	*xx*	*yy*
System Mass, (M_s)	**20.2 kg**	**17.5 kg**	**20.5 kg**	**17.6 kg**
Squeeze film inertia (M_{SFDyy})	**9.9 kg**	**7.2 kg**	**10.2 kg**	**7.3 kg**
R^2 (goodness of curve fit)	0.99	0.99	0.99	0.99
Predicted SFD inertia, M_{SFD}	**8.4 kg**			
Fluid Mass, (M_f) [kg]	0.62			
Housing Mass, (M) [kg]	9.7			

For predictions : ρ=800kg/m^3, η=2.8 10^{-3} Pa-s, K_{sx} = 853 kN/m, K_{sy} = 885 kN/m

Flow restrictor: 2.8 mm

Flow restrictor: 1.1 mm
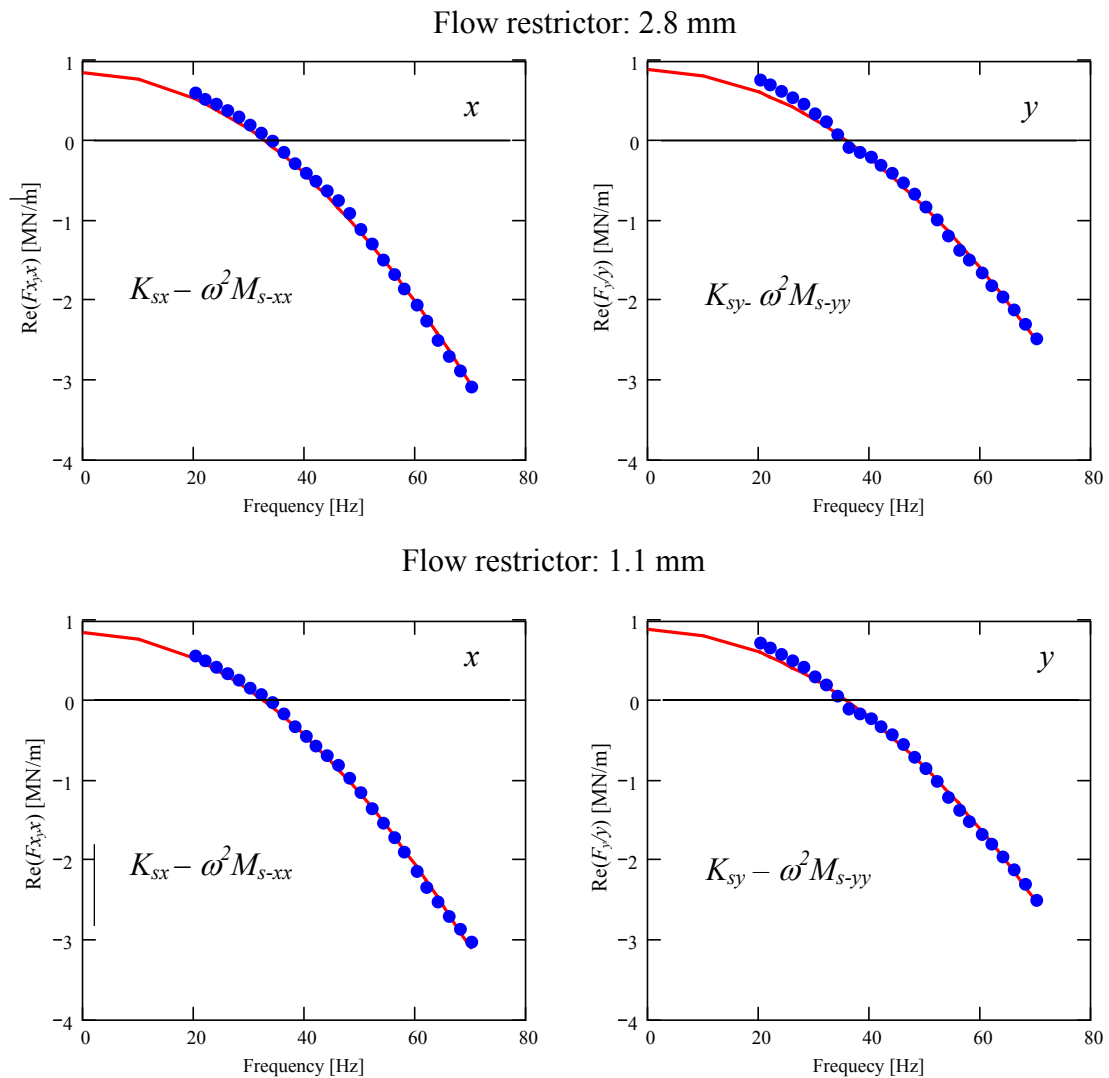
Figure 25 Real part of dynamic stiffnesses versus frequency. Circular centered orbits of amplitude *D*: 50 μm (K_{sx}= 853 kN/m, K_{sy}= 885 kN/m. 2.8 mm and 1.1 mm flow restrictors)

Figures 26 and 27 depict the test system direct damping coefficients ($C_{s\text{-}xx}, C_{s\text{-}yy}$) identified from tests at increasing orbit amplitudes (12 μm, 25 μm, 38 μm, 50 μm) for the two sets of flow restrictors (2.8 mm and 1.1 mm), respectively. The system damping coefficients, which include the squeeze film damper and dry friction from the mechanical seal, show a similar trend as those obtained form unidirectional load tests [2]; i.e. system damping decays steadily with excitation frequency. Furthermore, for the smallest amplitude (12 μm) the coefficient is significantly larger than those identified from larger motion amplitudes. This evidences the large influence of dry friction arising from the mechanical seal. Importantly enough, the dependency of the damping coefficient upon the amplitude of motion is less predominant as the excitation frequency increases. This is common in systems with dry friction. The size of the orifice discharge holes does not affect the damping coefficients since the squeeze film pressure fields do not show any signs of lubricant cavitation or air entrainment.

Figure 26 Identified test system direct damping coefficients (C_{s-xx}, C_{s-yy}) versus excitation frequency for increasing orbit amplitudes. (Circular Centered Orbits, lubricated SFD, 2.8 mm flow restrictors)
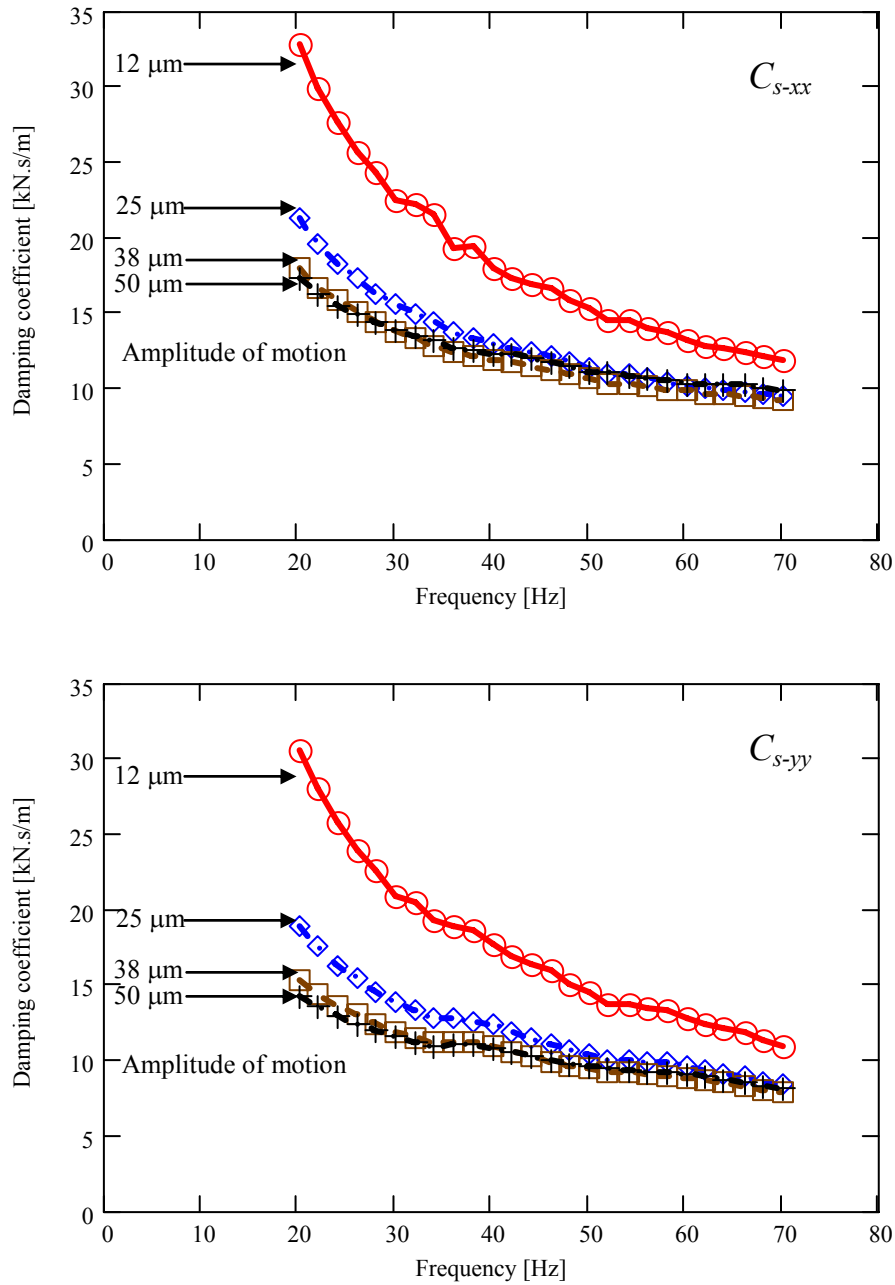
Figure 27 Identified test system direct damping coefficients ($C_{s\text{-}xx}$, $C_{s\text{-}yy}$) versus excitation frequency for increasing orbit amplitudes. (Circular Centered Orbits, lubricated SFD, 1.1 mm flow restrictor)

Figures 28 and 29 present the squeeze film coefficients (C_{SFDxx}, C_{SFDyy}) extracted from the system total damping coefficient ($C_{s\text{-}xx}$, $C_{s\text{-}yy}$) for both sets of flow restrictors. The coefficients shown follow from Eq. (18) and represent the squeeze film viscous damping contribution to the system overall damping. The squeeze film damping coefficients show a weaker dependency on frequency, which further confirms the significant contribution of

the dry friction interaction to the system overall damping coefficient. Unlike the C_{SFDyy} coefficients, the C_{SFDxx} coefficients show a certain level of frequency dependence. This dependency indicates that the damping contribution from the dry friction is being underestimated, especially at low frequencies. Notice that both sets of flow restrictor render similar squeeze film damping coefficients.
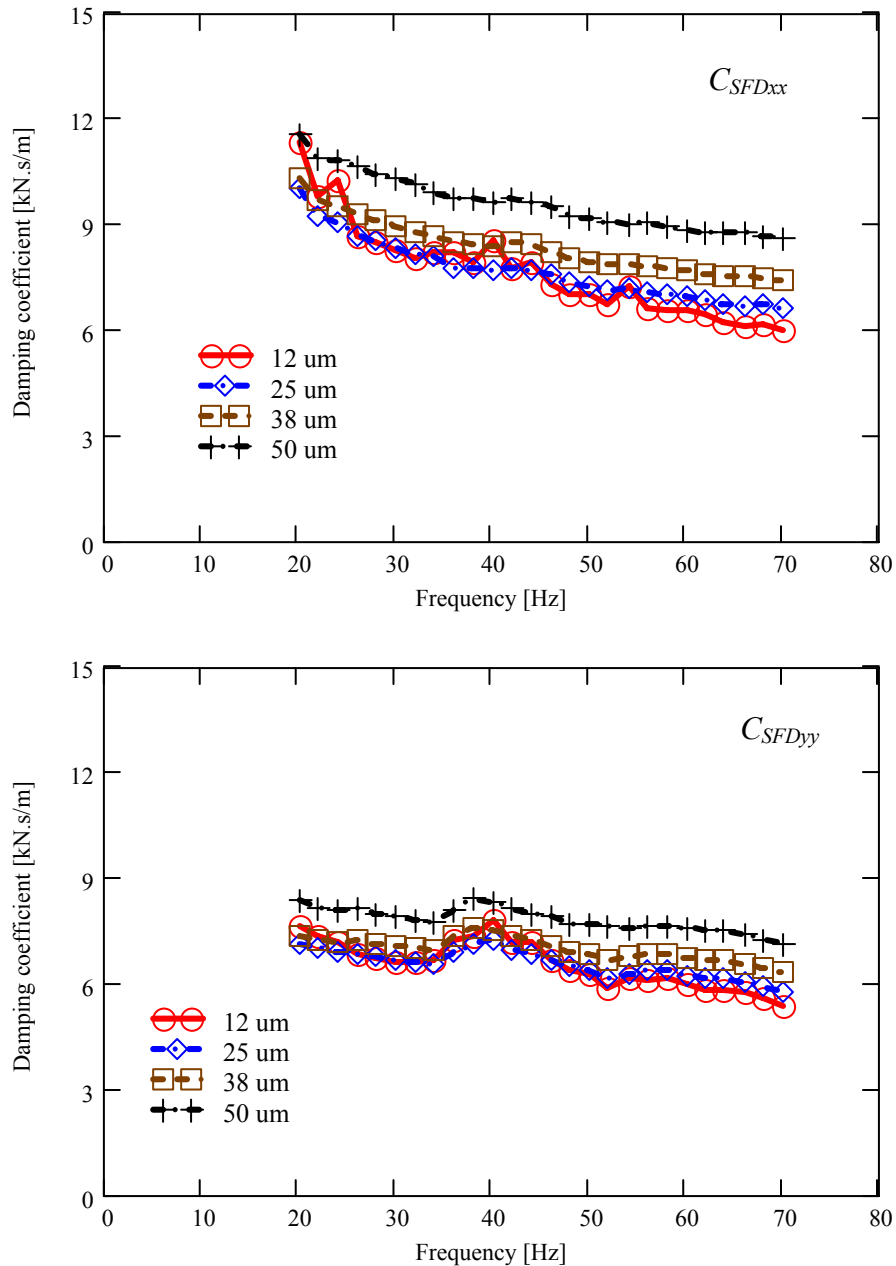
Figure 28 Squeeze film damping coefficients (C_{SFDxx}, C_{SFDyy}) versus excitation frequency for increasing orbit amplitudes. (Circular Centered Orbits, lubricated SFD, 2.8 mm flow restrictor)
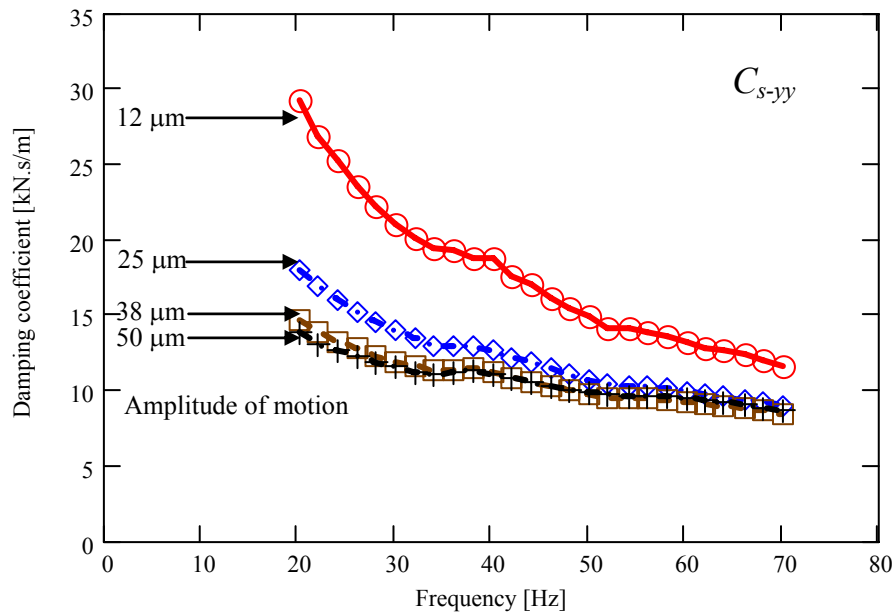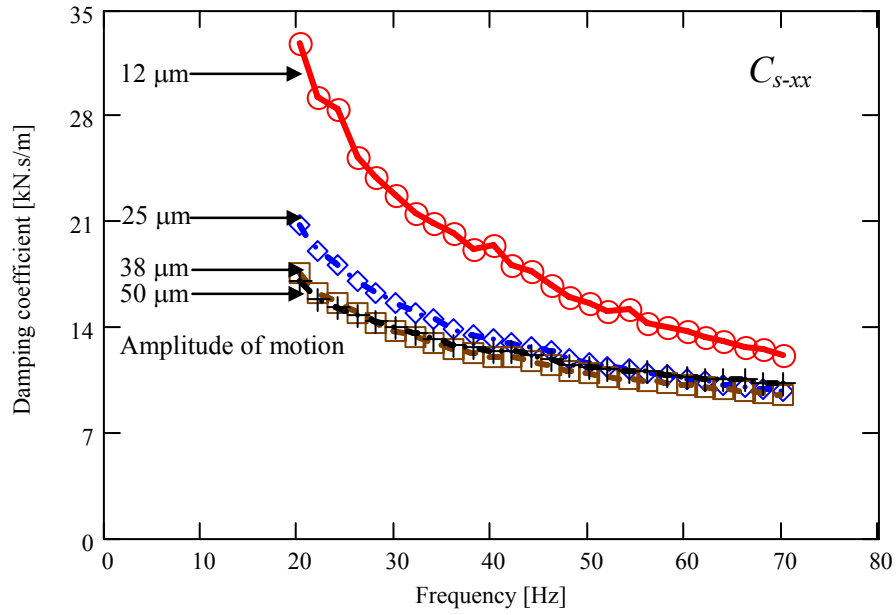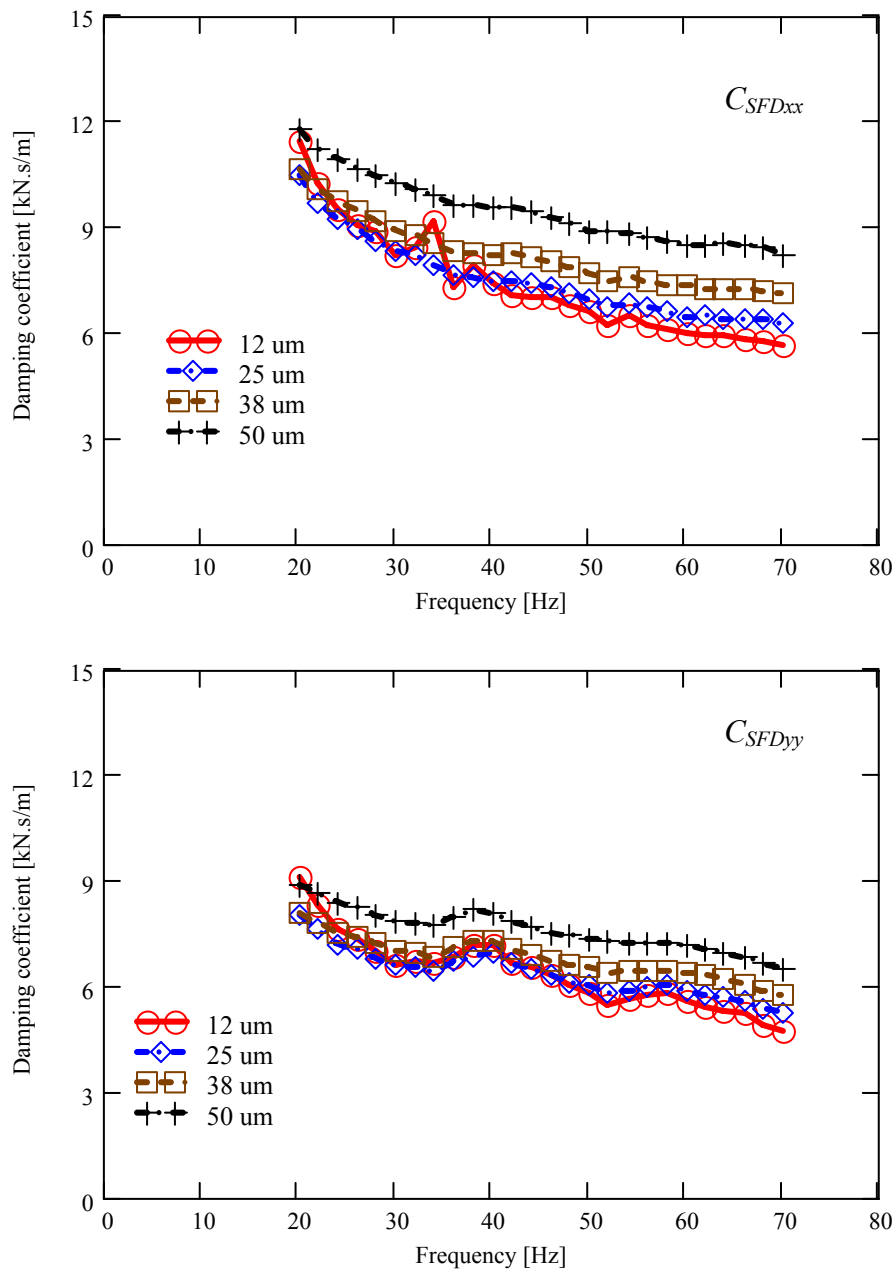
Figure 29 Squeeze film damping coefficients (C_{SFDxx}, C_{SFDyy}) versus excitation frequency for increasing orbit amplitudes. (Circular Centered Orbits, lubricated SFD, 1.1 mm flow restrictor)

Figures 30 and 31 depict the system damping coefficient (C_{s-xx}, C_{s-yy}) as a function of the amplitude of motion (radius or circular orbit). The dependency of the coefficients upon the displacement amplitude is more pronounced at low frequencies. Furthermore, the system damping coefficient for the smaller test amplitudes (12 μm) is larger than the damping recorded at any other amplitude level for all the frequencies tested. Once again, these trends are consistent with the effect of dry friction in the system.
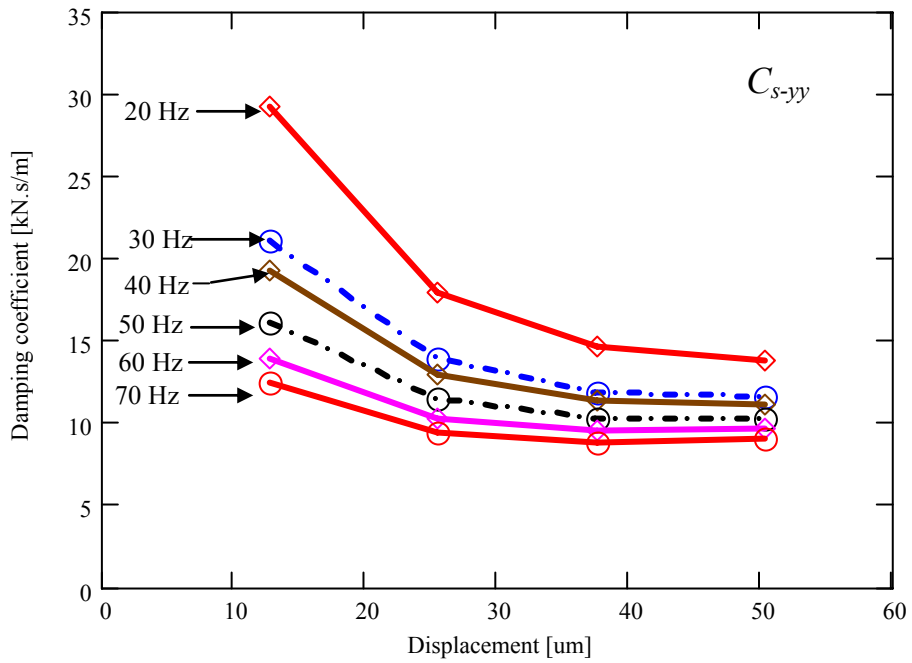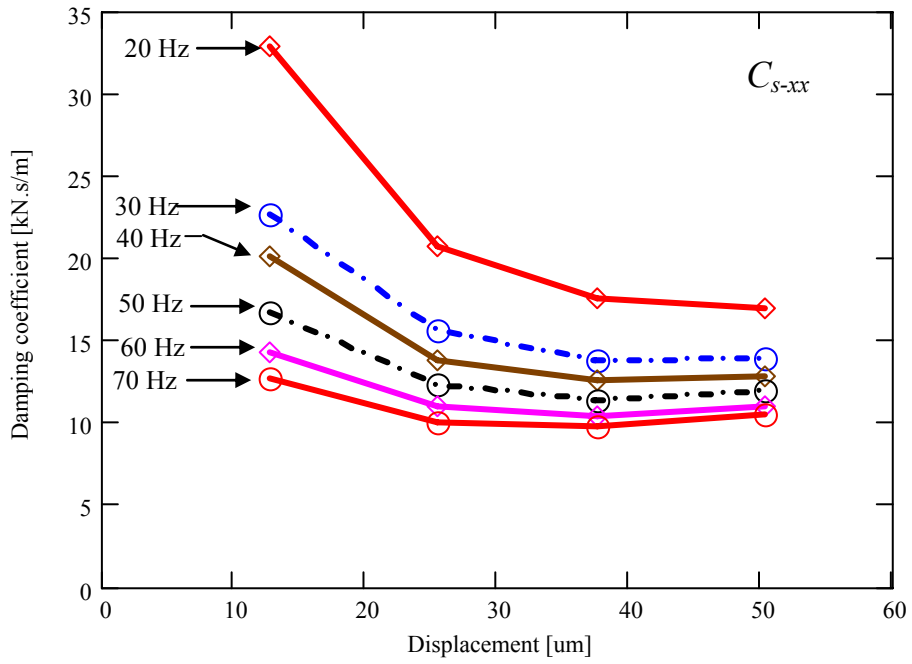
Figure 30 Identified system damping coefficients ($C_{s\text{-}xx}$, $C_{s\text{-}yy}$) versus orbit amplitudes for increasing frequencies. (Excitation frequency: 20 Hz, 30 Hz, 40 Hz, 50 Hz, 60 Hz and 70 Hz. Circular Centered Orbits, lubricated SFD, 2.8 mm flow restrictor)
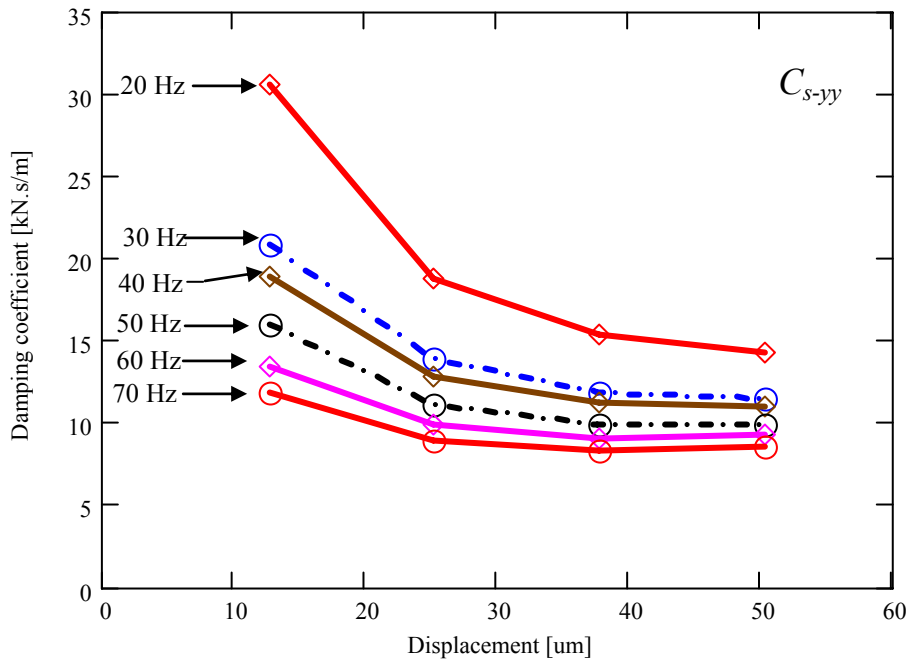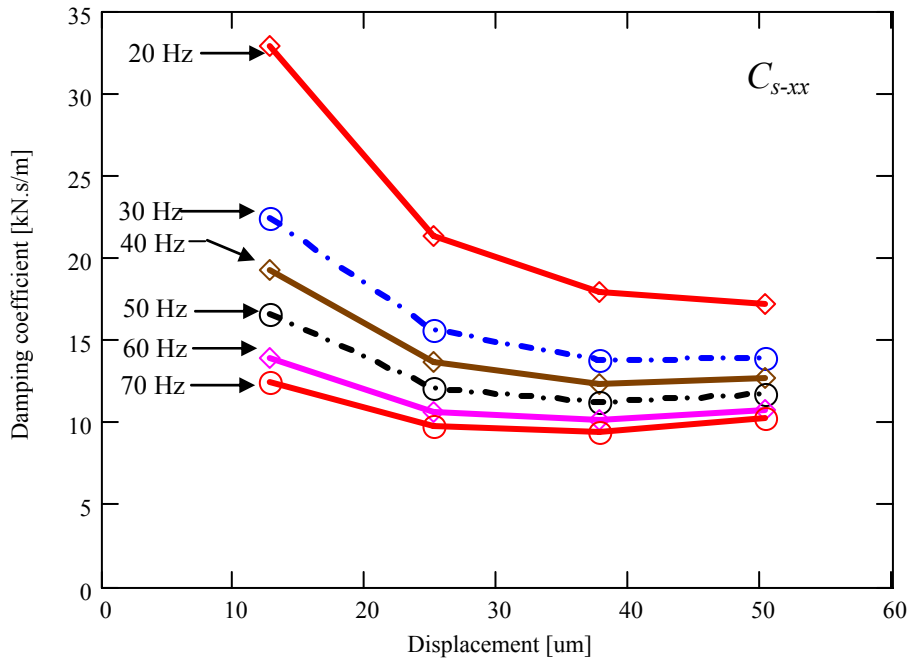
Figure 31 Identified system damping coefficients ($C_{s\text{-}xx}$, $C_{s\text{-}yy}$) versus orbit amplitudes for increasing frequencies. (Excitation frequency: 20 Hz, 30 Hz, 40 Hz, 50 Hz, 60 Hz and 70 Hz. Circular Centered Orbits, lubricated SFD, 1.1 mm flow restrictor)

Figures 32 and 33 illustrate the squeeze film damping coefficients (C_{SFDxx}, C_{SFDyy}) and predictions as function of the amplitude of motion for the two sets of flow restrictors (2.8 mm and 1.1 mm, respectively). The squeeze film viscous damping coefficients, as

opposed to the system damping coefficients, increase steadily with the amplitude of motion. For the 2.8 mm size restrictors, predictions underestimate by 20 % and 15% the experimental values along the X and Y directions, respectively. When using the 1.1 mm flow restrictors, the predictions are within 8% of the identified values for orbit amplitudes larger than 25 μm.

The test results show that both sealed SFD configurations, with 2.8 mm and 1.1 mm diameter flow restrictors, render similar damping coefficients (within 6 % in Y and 14 % in X) for the largest orbit amplitudes (50 μm). For the smaller amplitudes, at 25 μm orbit radius, the coefficients show a larger difference, up to 25 %. The discrepancy is attributed to the lower goodness of fit (R^2=0.97) when curve fitting Eq. (19) for the test results with small amplitudes of motion. The correlation factor R^2=0.99 for the test results obtained with the large 50 μm orbit radius.

Nevertheless, is important to note that the outlet flow area (3.8 mm^2) when using the smaller flow restrictor (1.1 mm diameter) is less that 15% of that associated to the 2.8 mm diameter flow restrictors (24.6 mm^2). Thus, the variation of the force coefficients due to the change of the flow restrictor diameters is relatively small. Therefore, the dynamic forced performance of the SFD presents a weak dependency on the flow discharge area of the outlet ports.
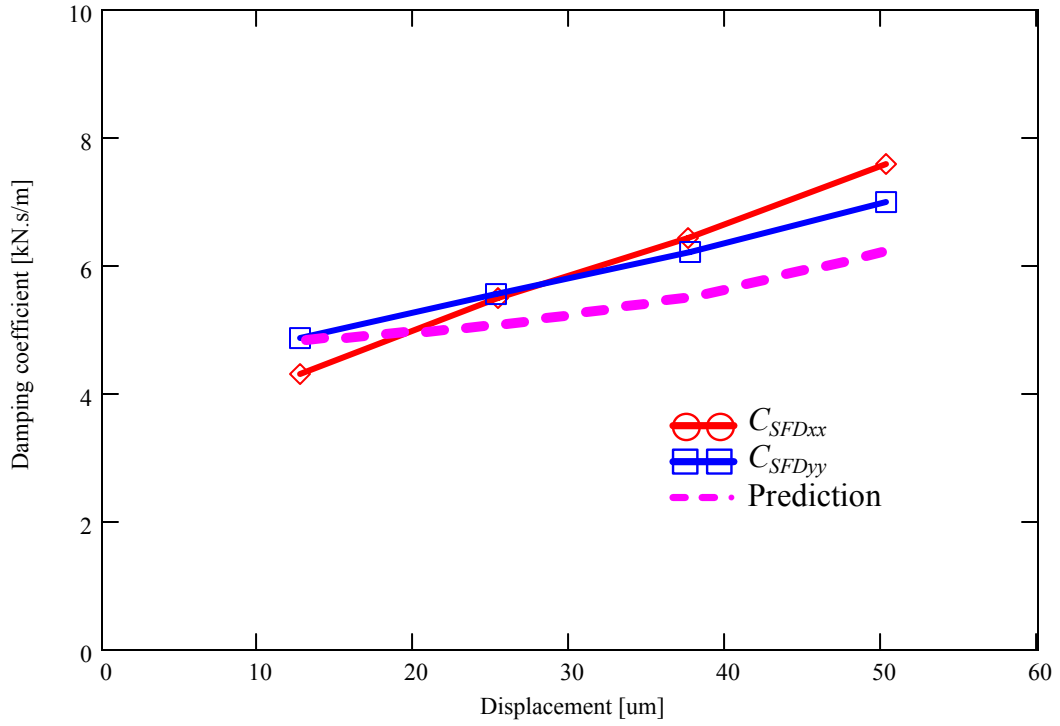
Figure 32 Squeeze film damping coefficients (C_{SFDxx}, C_{SFDyy}) versus orbit amplitude. (Circular Centered Orbits, Flow Restrictor: 2.8 mm)
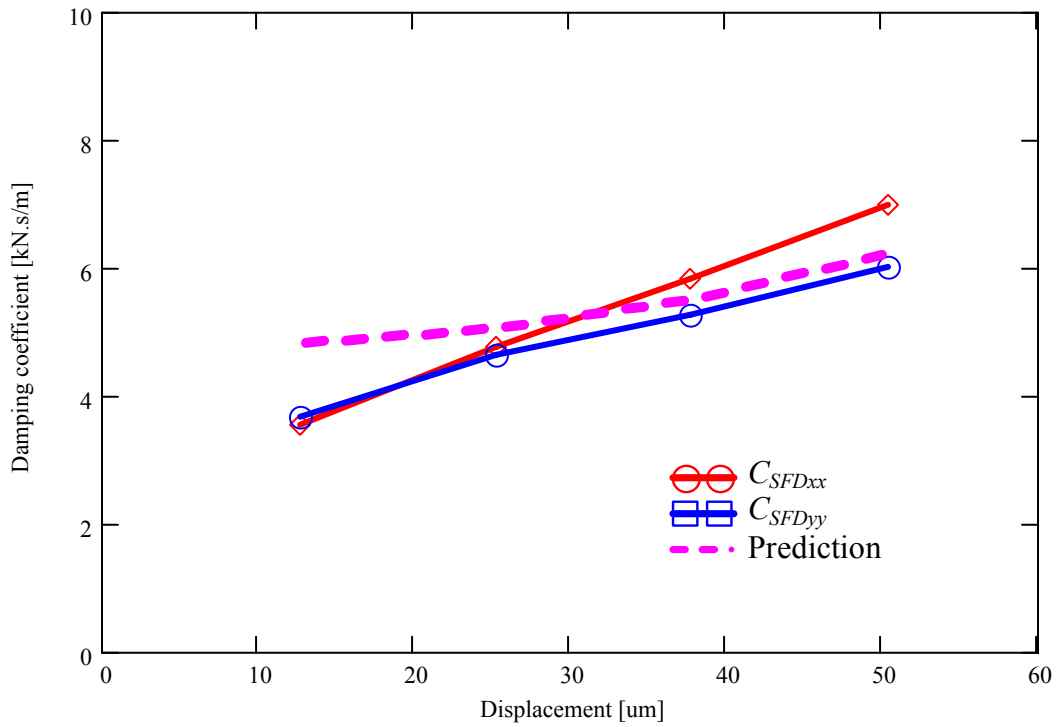
Figure 33 Squeeze film damping coefficients (C_{SFDxx}, C_{SFDyy}) versus orbit amplitude. (Circular Centered Orbits, Flow Restrictor: 1.1 mm)

VII Conclusions and Recommendations

The report describes tests and identification procedure to determine the damping and inertia force coefficients of a squeeze film damper and mechanical seal acting in parallel. Without the seal in place, static load tests determine the test system structural stiffnesses. Single frequency loads generating circular centered orbits on the dry (no lubricant) test system serve to identify, from a dissipated energy=work method, the dry friction force (34 N) at the seal contact surface. In the identification model, an equivalent viscous damping coefficient, amplitude and frequency of motion dependent, represents the dissipative action of dry friction in the mechanical seal.

With lubricant flowing through the SFD, test system damping and inertia force coefficients follow from dynamic load excitations also inducing circular centered motions in the frequency range from 20 to 70 Hz. Experiments are conduced using two sets of discharge flow restrictors (2.8 mm and 1.1 mm in diameter), which regulate the through lubricant flow and determine the levels of static and dynamic pressure in the recirculation annulus. The parameter identification is carried out in the frequency domain by building system transfer functions from the applied loads and measured dynamic displacements. The experimentally derived system damping coefficients combine the effects of dry friction in the seal contact zone, the squeeze film lands, and a residual action from the structural supports.

The identification results show that the system *viscous* damping coefficients are largest at the lowest frequency and smallest amplitude of orbital motions. The strong frequency dependency of the system damping coefficients indicates a substantial (equivalent) *viscous* damping from dry friction in the mechanical seal. Predicted squeeze film damping coefficients, based on the short length bearing model, agree well (within 15 %) with the experimental results except for the C_{SFDxx} coefficients, being slightly underestimated (20 % difference). The predicted fluid inertia coefficient lies within 16 % of the test identified coefficient, provided that twice the film length is used in the predictive formula.

The experiments demonstrate that for both sets of flow restrictors, the mechanical end seal effectively prevents air ingestion and entrapment into the squeeze film land for the

frequencies and amplitudes of motion tested. Furthermore, the coefficients obtained for both restrictor hole sizes are similar, as expected.

Future work will include tests without through flow by closing the discharge ports. The results from this and future experiments will aid to validate analytical developments focused on improving predictions of inertia force coefficients (added mass terms) in squeeze film dampers.

VIII References

[1] Zeidan, F.Y., San Andrés, L., and Vance, J. M., 1996, "Design and Application of Squeeze Film Dampers in Rotating Machinery," *Proc. 25th Turbomachinery Symposium*, Houston, TX, pp.169-188.

[2] Delgado, A., and San Andrés, L., 2004, "Sealed end Squeeze Film Damper: Test rig Description and Identification of Structural Parameters," TRC report, TRC-SFD-1-05, May.

[3] Pietra, D., and Adiletta, G., 2002,"The Squeeze Film Damper over Four Decades of Investigations. Part I: Characteristics and Operating Features," The Shock and Vibration Digest, **34**(1), pp. 3-26.

[4] Pietra, D., and Adiletta, G., 2002,"The Squeeze Film Damper over Four Decades of Investigations. Part II: Rotordynamic Analyses with Rigid and Flexible Rotors," The Shock and Vibration Digest, **34**(2), pp. 97-126.

[5] Roberts, J. B., Holmes, H., and Mason, T. J., 1986, "Estimation of Squeeze-Film Damping and Inertial Coefficients from Experimental Free-Decay Data," Proc. Inst. Mech. Eng. Part C, **200**(C2), pp. 123-133.

[6] Ellis, J., Roberts, J. B., and Hosseini, S. A., 1990, "The Complete Determination of Squeeze-Film Linear Dynamic Coefficients from Experimental Data," ASME J. of Tribol., **112**(4), pp. 712-724.

[7] Yu, S., and Rogers, R., 1991, "Estimation of Linearized Force Coefficients for Cylindrical Squeeze Film Dampers," ASLE Tribol. Trans., **34**(2), pp. 308-317.

[8] Zhang, J., Roberts, J. B., and Ellis, J., 1994, "Experimental Behavior of a Short Cylindrical Squeeze Film Damper Executing Circular Centered Orbits," ASME J. of Tribol., **116**(3), pp. 528-534.

[9] Diaz, S., and San Andrés, L., 2000, "Orbit-Based Identification of Damping Coefficients of Off-Centered Squeeze Film Damper Including Support Flexibility," ASME Paper No. 2000-GT-0394.

[10] Della Pietra, L., 2000, "Analytical and Experimental Investigation of Squeeze-Film Dampers Executing Circular Orbits," Meccanica, **35**(2), pp. 133-157.

[11] San Andrés, L., 1996, "Theoretical and Experimental Comparisons for Damping Coefficients of a Short Length Open-End Squeeze Film Damper," ASME Journal of Engineering for Gas Turbines and Power, Vol. 118, 4, pp. 810-815.

[12] San Andrés, L., Vance, J. M., 1987, "Effects of Fluid Inertia on Finite-Length Squeeze Film Dampers," ASLE Trans., **30**(3), pp. 384-393.

[13] Levesley, M., and Holmes, R., 1996, "The Effect of Oil Supply and Sealing Arrangements on the Performance of Squeeze-Film Dampers: an Experimental Study," J. Eng. Tribol. Part J, **210**(4), pp. 221-232.

[14] De Santiago, O., and San Andrés, L., 1999, "Imbalance Response and Damping Force Coefficients of a Rotor Supported on End Sealed Integral Squeeze Film Dampers," ASME Paper 99-GT-203.

[15] Kim, K., and Lee, C., 2005, "Dynamic Characteristics of Sealed Squeeze Film

Damper with a Central Feeding Groove," ASME J. of Tribol., **127**(1), pp. 103-111.

[16] Diaz, S., and San Andrés, L., 2001, "A Model for Squeeze Film Dampers Operating with Air Entrainment and Validation with Experiments," ASME J. of Tribol., **123**(1), pp. 125-133.

[17] San Andrés, L., and De Santiago, O., 2004, "Forced Response of a Squeeze Film Damper and Identification of Force Coefficients from Large Orbital Motions," ASME J. of Tribol., **126**(2), pp. 292-300.

[18] San Andrés, L., Diaz, S., and Rodriguez, L., 2001, "Sine Sweep Load Versus Impact Excitations and their Influence on the Damping Coefficients of a Bubbly Oil Squeeze Film Damper," ASLE Tribol. Trans., **44**(4), pp. 692-698.

[19] Diaz, S., 2000, " CCO Data adquisition," LabView® Virtual Instrument. Texas A&M University, Tribology Group.

[20] Delgado, A., and San Andrés, L., 2004, "Sealed end Squeeze Film Damper: Test rig Description and Identification of Structural Parameters," TRC report, TRC-SFD-1-04, May.

[21] Ginsberg, J. H., 2001, *Mechanical and Structural Vibrations*, John Wiley & Sons, *Inc*., New York, pp. 135-139.

[22] Pinkus, O., and Sternlight, B., 1961, *Theory of Hydrodynamic Lubrication,* McGraw-Hill Book Company Inc. , New York. pp. 34-35

[23] Efunda, 2006, "Orifice Flowmeters," http://www.efunda.com/fluids/formulae/cals-orifice.cfm

[24]San Andrés, L., 2005, "An Improved Model for Prediction of Fluid Inertia Coefficients in SFDs and Annular Seals," Internal Communication, Tribology Group, Texas A&M Univ., Turbomachinery Laboratory, January.

[25] Coleman, H. W., and Steele, G. W., 1988, *Experimentation and Uncertainty Analysis for Engineers,* John Wiley & Sons, New York. Chapters 1-4.

Appendix A Identification of Test System Structural Stiffness and Mass

The appendix presents the re-estimation of the test system structural parameters. The system parameters were previously identified in [2], but the current system was slightly modified to correct certain issues concerning to the motion of the main frame structure (See Figure 1). In particular, the main frame structure was stiffened using steel plates and additional supports attaching the top plate to the bottom of the rig. The natural frequency of the main support structure increased from ~50 Hz to ~150 Hz. The identification of the structural parameters follows.

A.1 Static tests

The experimental procedure and estimated mass of the SFD assembly is reported in [2]. The results are presented in Table A1.

Table A1 Measured weight and estimated effective mass of the SFD assembly and connecting rods.

	Weight
SFD Assembly [±0.01] *	6.4 kg
Lid and hose connector**	3 kg
Rods [±0.001]	0.59 kg
Blocks[±0.001]	0.11 kg
Total effective mass	9.7 kg (±1%)

*: including hose connectors, ring carrier and sensors.
**: including pressure sensor.

Static load tests using a force gauge (±0.5 lb) and two eddy current sensors (*X2,Y2*) yield two stiffness parameters (K_{sx}, K_{sy}). These tests are conducted without the journal in position (i.e. no rubbing interface). Figure A 1 shows the bearing deflections in the *X* and *Y* directions due to a force exerted in the same direction. Each data point represents an average of a set of two static load tests. The results follow a linear tendency along the entire range of loads exerted on the SFD assembly (-120 N to 120 N). Thus, a uniform structural stiffness coefficient in each direction (*X* and *Y*) is appropriate to characterize the flexibility of the four rods arrangement.
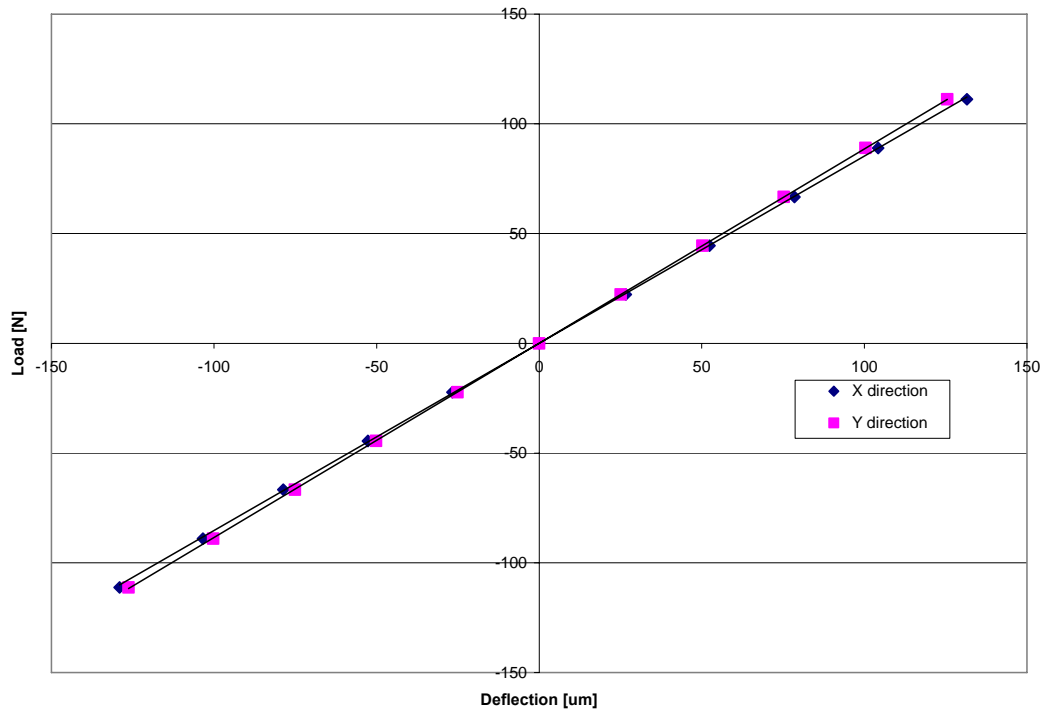
Figure A 1 Bearing deflection vs. applied load in the *X,Y* direction due to a force applied in the respective (same) direction. (*U_F*: 2.2 N)

Table A2 presents the structure stiffnesses in the *X* and *Y* directions. The values are in both directions are similar (~4% different), thus confirming the symmetry of the test element.

Table A 2 Structural stiffnesses of support from static load tests

	K_{sx}[N/m]	K_{sy}[N/m]
Value	853 x10^3	885 x10^3
Uncertainty	34 x10^3[~4%]	35 x10^3[~4%]
Range[N]	-110 to 110	-110 to 110
f_n* [Hz]	47±1	48±1

*: obtained using the stiffnesses and weight measured from static tests

A. 2 Impact tests

A sets of impact tests performed along the *X* and *Y* directions of the SFD assembly stand to identify the structural parameters of the SFD assembly. Figures A2 and A3 show the system transfer functions in the *X* and *Y* directions obtained from the impact test, respectively. Table A3 presents the results from the impact tests exerted on the bearing assembly.
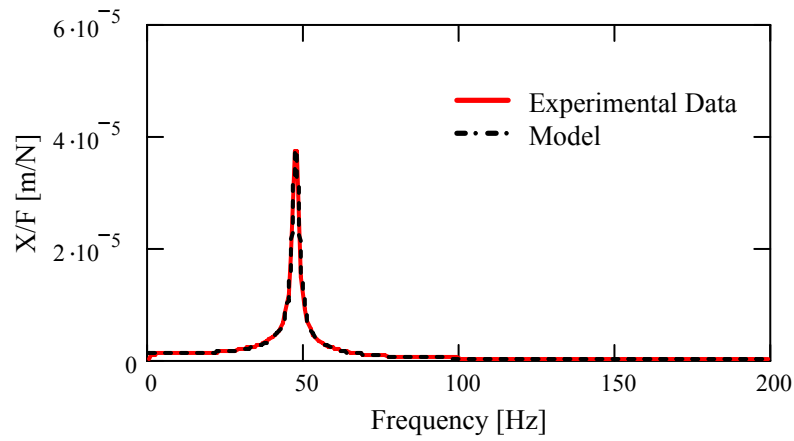
Figure A 2 Impact tests transfer function and analytical fit for motions along *X* direction. (Dry system, end seal not in place)
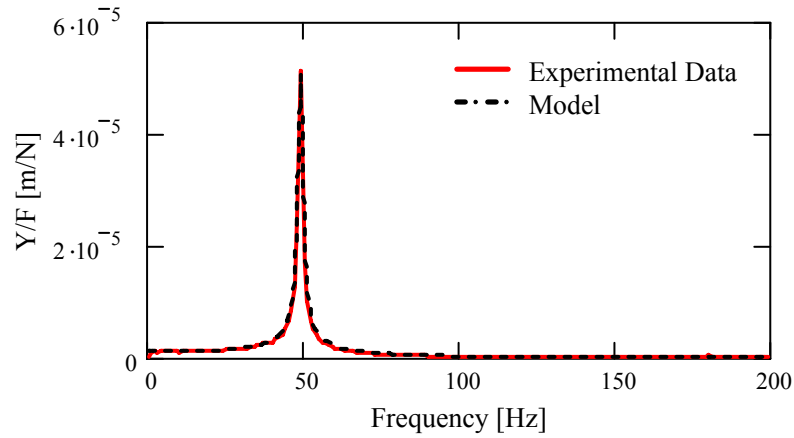
Figure A 3 Impact tests transfer function and analytical fit for motions along *Y* direction. (Dry system, end seal not in place)

Table A 3 Identified parameters from impact tests exerted on SFD test section (no lubricant)

	Parameters	*X*	*Y*
	Stiffness, K_s [kN/m]	884 (±45)	929 (±50)
SI	Mass, M [kg]	9.9 (±0.5)	9.8 (±0.5)
	Damping, C_s [N.s/m]	65	58
	Damping ratio, ζ	0.011	0.01
	Natural Frequency f_n[Hz]	48 ±1	49 ±1
	R^2 (goodness of fit)	0.99	0.99

The mass estimated from the static tests (measured weight and static stiffness) is in agreement with the values obtained from impact tests in the X direction (~2%) and Y direction (~1%). The stiffness estimated from impact tests are similar (within ~5%) to the one obtained from static test in the both directions..

For identification purposes, the stiffness of the test system is taken from the static load tests (uncertainty band 4%), i.e. K_{sx} = 853 kN/m, and K_{sy} =885 kN/m.

Appendix B Uncertainty analysis of test data

The appendix presents the uncertainty associated with the results reported. The analysis contemplates the estimation of the error of each individual measurement, as well as the error propagation associated with parameters that are function of other variables.

B.1 Parameter Identification

B.1.1 Static tests

The procedure to estimate uncertainty of the stiffness resulting from static test is similar to the one followed in the calibration of the proximity sensor. In this case, since each data pair (displacement, force) is the average from three different tests, the uncertainty of each point (in the displacement axis) of the force vs. displacement data collection is given by the combination of the instrument uncertainty (i.e. voltmeter) and the error incurred from averaging the three test, which is given by

$$U_{avg} = tS_{\bar{x}} \ \ t=4.303, \quad S_{\bar{x}} = S_x / \sqrt{N} \quad ; \ S_x = \left[\frac{1}{N-1}\sum_{i=0}^{N}(X_i - \bar{X})^2\right]^{1/2} \tag{B.6}$$

where $S_{\bar{x}}$ is the precision index of the mean value, S_x is the precision index; and, $\bar{X}$ and X_i represent the mean of the sample array and the individual samples, respectively. And t is the coefficient for 2 degrees of freedom (N-1) and a 95% confidence interval for a t-distribution of data points [25].

Subsequently, the uncertainty of the linear fit is given by B.1 and the uncertainty associated with the slope (stiffness coefficient) is defined as

$$\left(\frac{U_K}{K}\right)^2 = \left(\frac{1}{\Delta F}U_F\right)^2 + \left(\frac{1}{\Delta D_{fit}}U_{D_{fit}}\right)^2 + \left(\frac{1}{G}U_G\right)^2 \tag{B.7}$$

where

$$K = \frac{G}{V}F \tag{B.8}$$

B.1.2 Impact tests

For this case, the uncertainty in the stiffness and mass coefficients is given by the uncertainty associated with the measurements of displacement and force (i.e. instrumentation uncertainty) and the error from the transfer function fit.

$$H(\omega) = \frac{1}{\left[\left(K^2 - M\omega^2\right)^2 + (C\omega)^2\right]^{1/2}} \tag{B.9}$$

This assumption is valid for stiffness and mass coefficient only, regarding that the curve fit matches the measured flexibility (i.e. displacement/ force) at $\omega \to 0$ ($\pm 4\%$), and that the stiffness and the mass given by the numerical fit follow from the expressions

$$H_{fit}(0) = \frac{1}{K}, \quad M = \frac{K}{\omega_n^2} \tag{B.10}$$

where the uncertainty of the natural frequency ω_n is given by the window resolution used in the dynamic frequency analyzer (400 Hz/400 lines= $\pm$ 1Hz resolution).
Therefore, the uncertainties of the stiffness and mass are

$$\frac{U_K}{K} = \frac{U_{H_{fit}}}{H(0)}, \quad \left(\frac{U_M}{M}\right)^2 = \left(\frac{U_K}{K}\right)^2 + \left(\frac{2U_K}{\omega_n}\right)^2 \tag{B.11}$$

where

$$\left(\frac{U_{H_{fit}}}{H_{fit}}\right)^2 = \left(\frac{U_F}{F}\right)^2 + \left(\frac{U_D}{D}\right)^2 + \left(1 - \frac{H}{H_{fit}}\right)^2$$

and

$$\left(\frac{U_F}{F}\right) = 0.01 \text{ (1\% linearity)}, \quad \left(\frac{U_D}{D}\right)^2 = \left(\frac{0.0008}{.03019}\right) = 7.84x10^{-4}$$

B.2   Flow Measurements

The flow meter is rated for flows from .3 to 3 GPM, and is field calibrated to ensure greater accuracy. The calibration procedure requires a container calibrated in one gallon increments from one to five. The container is calibrated by weighing water to estimate its volume as

$$gal._{h_2o} = Mass * \left(\frac{1}{\rho h_2 0}\right) * \left(\frac{1}{Cp}\right) \tag{B.12}$$

where mass as the liquid mass, ρ the density of water at 21 ^{0}C and Cp a conversion factor conversion factor (0.13368 ft^3/gal. h20)

The uncertainty of Eq. B.1 is related to the dynamometer used to weight the water and is given by the expression [25]

$$Ucalib. = \left[\left(\frac{\partial gal.}{\partial Mass} * Umass \right)^2 \right]^{1/2} \qquad \text{(B.13)}$$

The uncertainty of the calibration of the container is 0.03 gallons.

Field calibration of the flow meter involves reading the amount of liquid in the container and inputting the data into the flow meter. The level of liquid in the calibration container can be read at an accuracy of 1/16" from the actual gallon mark. The combined error of the calibration is 0.04 Gal. The bias error of the flow meter is given by the manufacturer as %1.5 of the measured value.

Pressure is measured using Omega® PX-215 pressure sensors. The sensors operate on a process current from 4 to 20mA. This current is read by a digital ammeter before entering the Omega® display. The current output of the pressure sensors was calibrated to pressures using an Ashcroft portable gauge tester. The current measured is converted to pressure using equation

$$P = k * ip + C_2 \qquad \text{(B.14)}$$

where k is the pressure sensor calibration constant, ip the measured current (mA) and C_2 intercept of pressure calibration curve

The equation for the pressure sensor calibration constant is given by

The uncertainties used in this analysis were the uncertainty of the Ashcroft portable tester and the digital ammeters. The uncertainty values for the pressure sensors at the inlet and recirculation annals are calculated at 5 psig. The uncertainty of the calibration (Eq. B.3) is given by [25]

$$Uk = \left[\left(\frac{\partial k}{\partial P} * UP_{calib.} \right)^2 + \left(\frac{\partial k}{\partial ip} * Uip \right)^2 \right]^{1/2} \qquad \text{(B.15)}$$

Combining the uncertainty of the calibration and the uncertainty of the ammeter reading yields the uncertainty of the pressure measurement

$$Up = \left[\left(\frac{\partial P}{\partial k} * Uk \right)^2 + \left(\frac{\partial P}{\partial ip} * Uip \right)^2 \right]^{1/2} \qquad \text{(B.16)}$$

The uncertainty of the inlet pressure reading is 0.182 psig. The uncertainty of the pressure readings at the recirculation annulus is 0.177 psig.

For the flow measurements the precision index for each sample is calculated as [25]

$$S_X = \left[\frac{1}{N-1} \sum_{i=1}^{N} \left(X_i - \overline{X} \right)^2 \right]^{1/2}$$ (B.17)

and the precision index of the mean is

$$S_{\overline{X}} = S_X / \sqrt{N}$$ (B.18)

where N is the number of samples , X is the sample values and $\overline{X}$ is the mean value of the sample population. The t value for %95 confidence with three samples is 4.3. The precision error is [25]

$$P_{\overline{X}} = t S_{\overline{X}}$$ (B.19)

The bias error is a combination of the calibration errors and the manufacturer given %1.5 bias error.

Figure B.1 shows the average of the set flow measurements versus supply pressure. The error band of the measurements is noted with dotted lines.
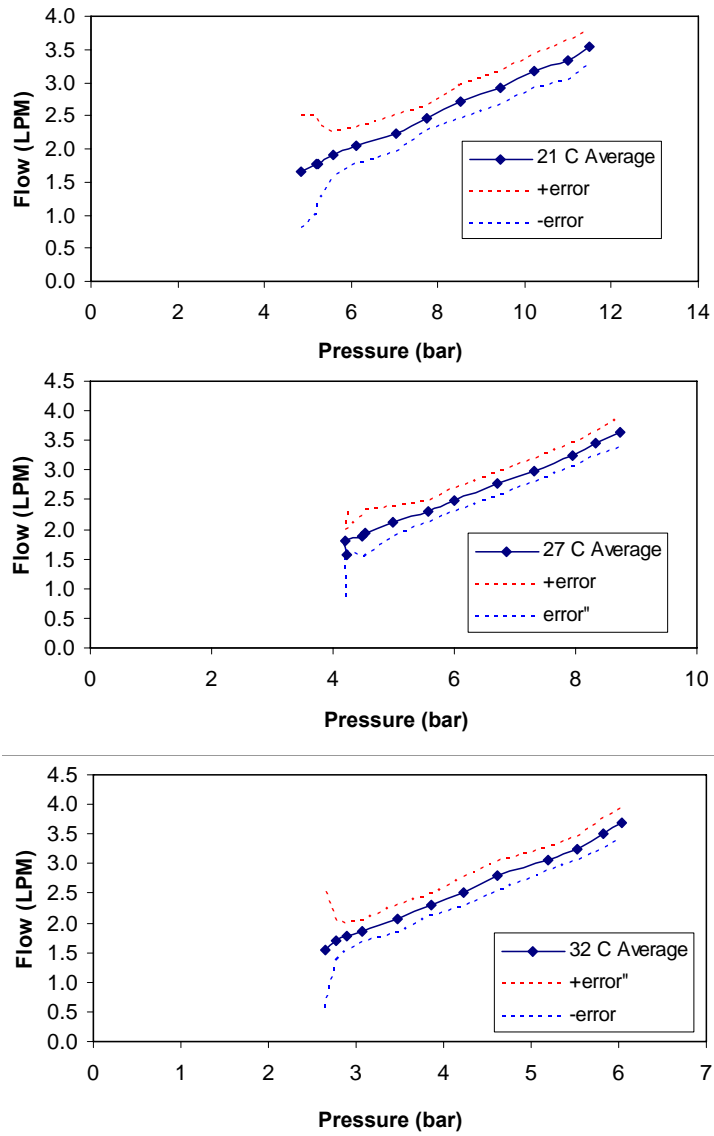
Figure B 1 Lubricant flow through SFD versus supply pressure. (Average from flow measurements for three temperatures 21 C, 27 C, 32 C)

Appendix C Recorded orbits for loads and damper motion (displacement and acceleration) at 20 Hz, 40 Hz, 60 Hz

The appendix presents figures displaying the *Y* versus *X* loads (top left), ensuing bearing displacements (top right) and acceleration (bottom graphs) orbits obtained for the circular centered orbit tests at 20 Hz, 40 Hz and 60 Hz. The displacement orbits are nearly circular (as intended) while the load orbits are somewhat elliptical, with the major axis along the *X* direction. The acceleration orbits are only noticeable at high frequencies.
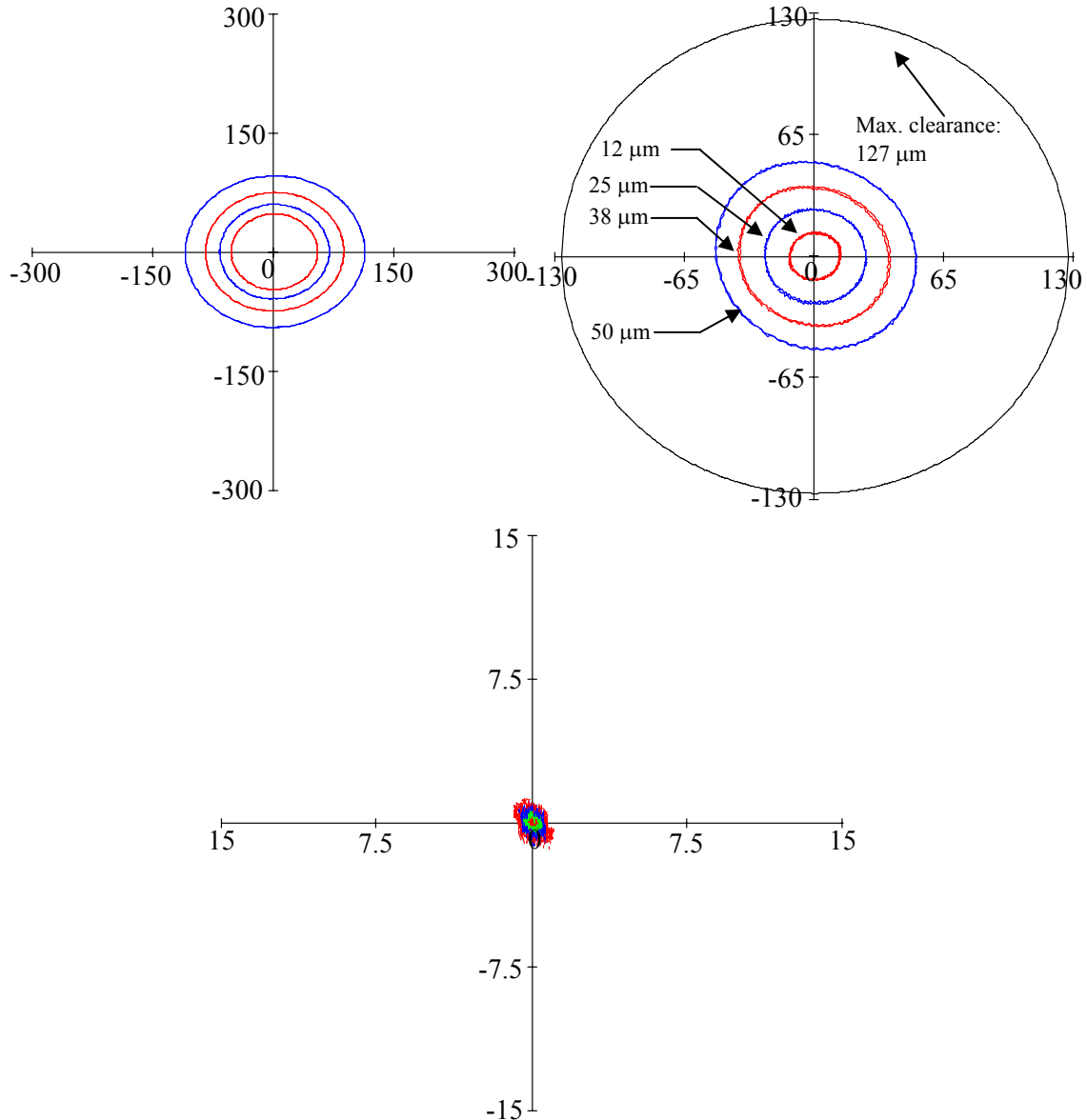

Figure C 1 Excitation load and response orbits (motion and acceleration) from experimental data. (20 Hz, Flow restrictor: 2.8 mm, Load: [N], Acceleration [m/s2], displacement [μm])
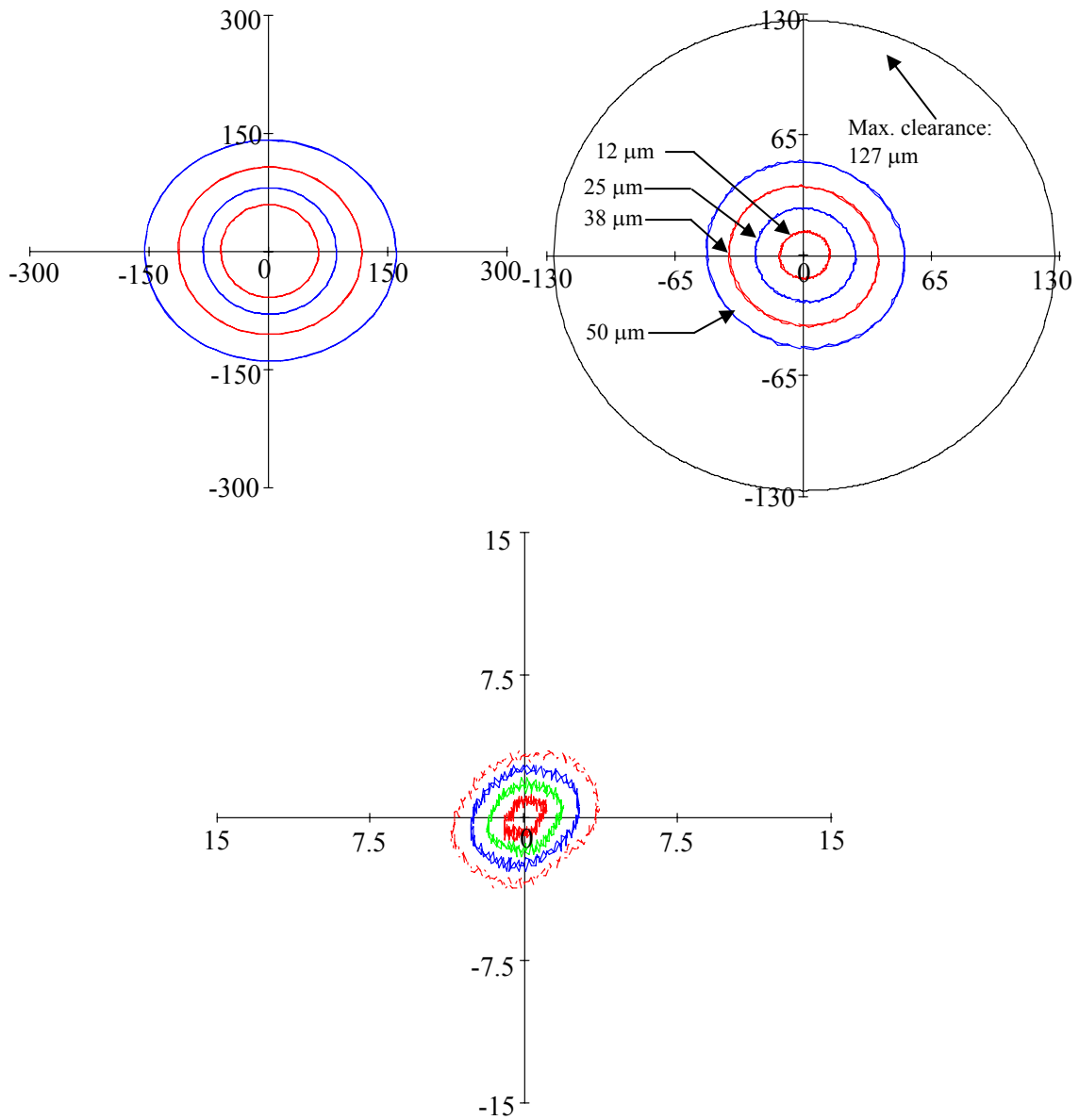
Figure C 2 Excitation load and response orbits (motion and acceleration) from experimental data. (40 Hz, Flow restrictor: 2.8 mm, Load: [N], Acceleration [m/s2], displacement [μm]))
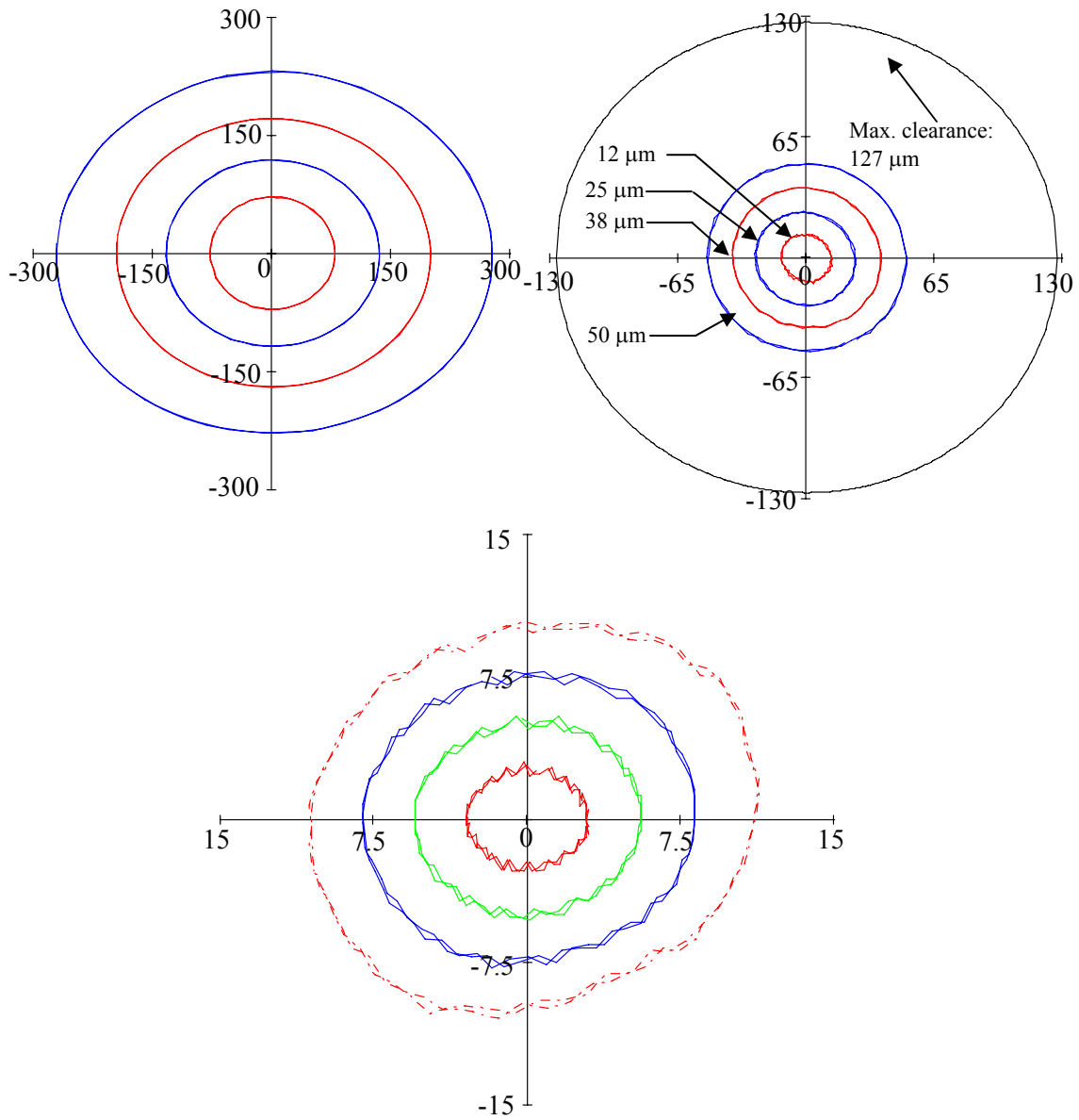
Figure C 3 Excitation load and response orbits (motion and acceleration) from experimental data. (70 Hz, Flow restrictor: 2.8 mm, Load: [N], Acceleration [m/s2], displacement [μm]))
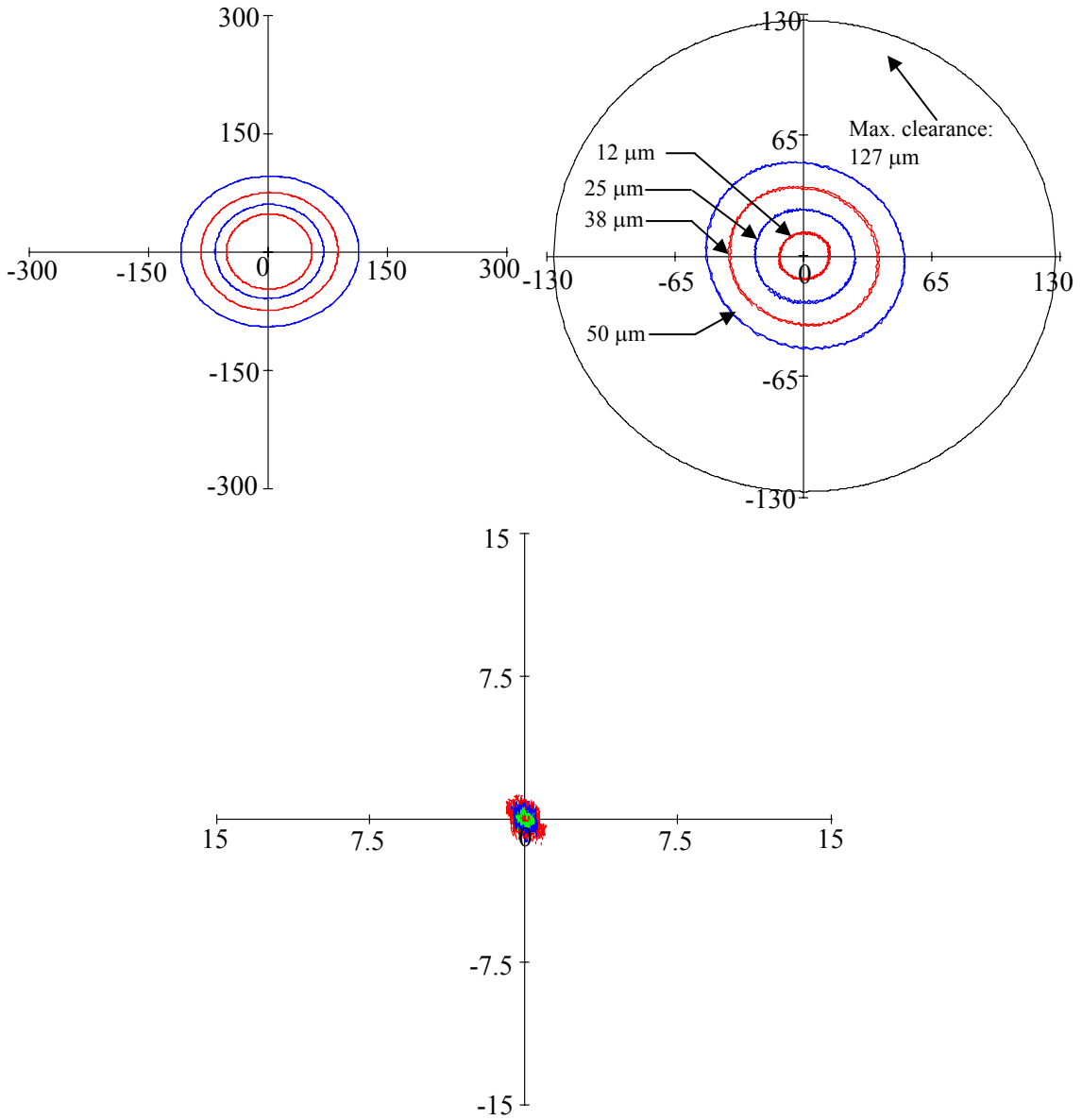
Figure C 4 Excitation load and response orbits (motion and acceleration) from experimental data. (20 Hz, Flow restrictor: 1.1 mm, Load: [N], Acceleration [m/s2], displacement [μm]))
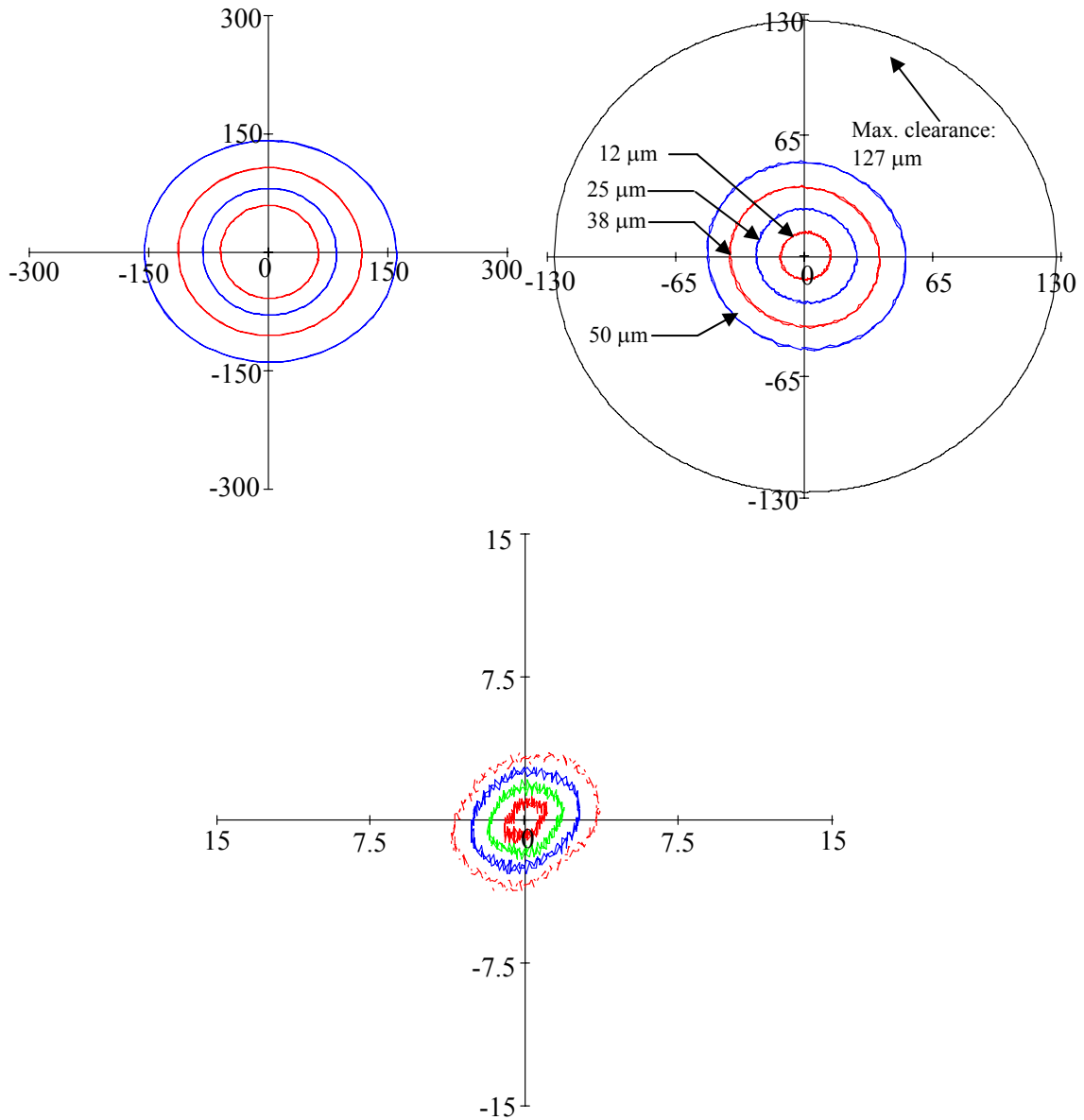
Figure C 5 Excitation load and response orbits (motion and acceleration) from experimental data. (20 Hz, Flow restrictor: 1.1 mm, Load: [N], Acceleration [m/s2], displacement [μm]))
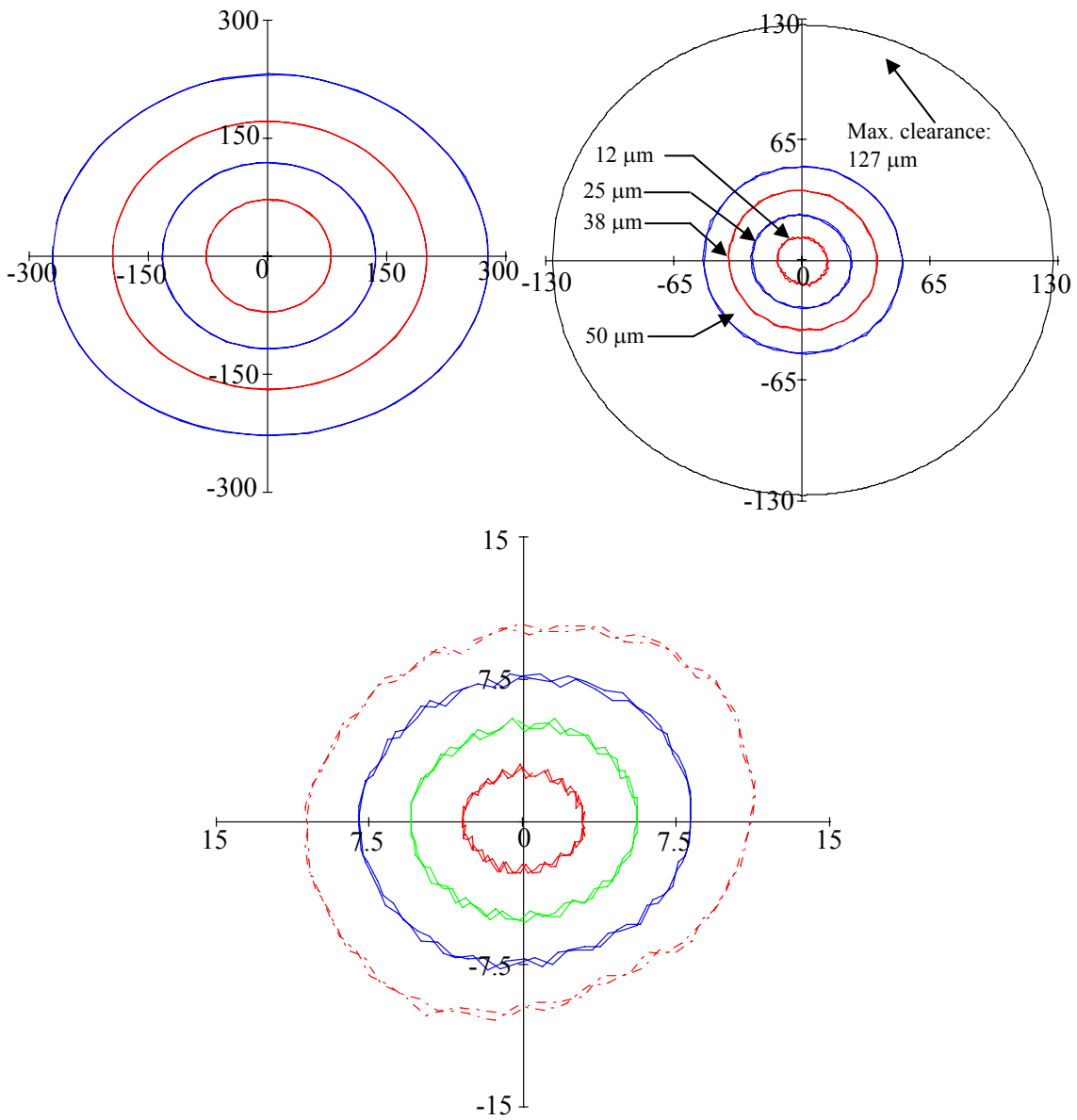
Figure C 6 Excitation load and response orbits (motion and acceleration) from experimental data. (70 Hz, Flow restrictor: 1.1 mm, Load: [N], Acceleration [m/s2], displacement [μm]))

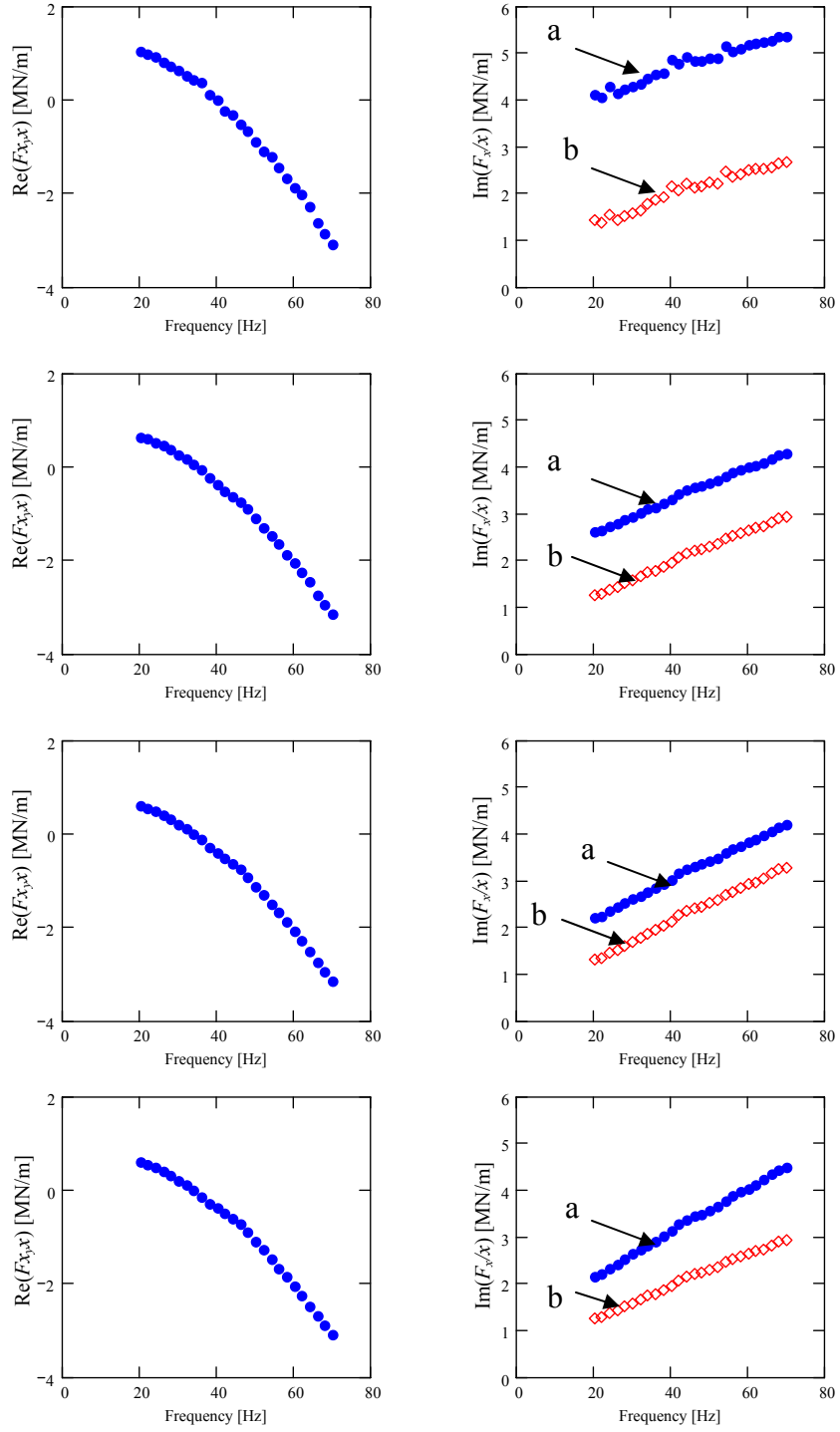## Appendix D Real and Imaginary Components of Complex Dynamic Stiffnesses

The appendix presents figures displaying the experimentally derived real and imaginary parts of the complex dynamic stiffnesses ($\left(\dfrac{\overline{F}_x}{x}\right)$, $\left(\dfrac{\overline{F}_y}{y}\right)$) for the lubricated test system with the 2.8 mm and 1.1 mm diameter size flow restrictors. Note that the graphs on the imaginary part of the dynamic impedance also include results for the expressions

$$\omega\, C_{SFD_{xx}} = \text{Im}\left(\dfrac{\overline{F}_x}{x}\right) - \dfrac{F_\mu}{|\overline{x}|} - \omega\, C_{rv}$$

$$\omega\, C_{SFD_{yy}} = \text{Im}\left(\dfrac{\overline{F}_y}{y}\right) - \dfrac{F_\mu}{|\overline{y}|} - \omega\, C_{rv}$$

(D.1)

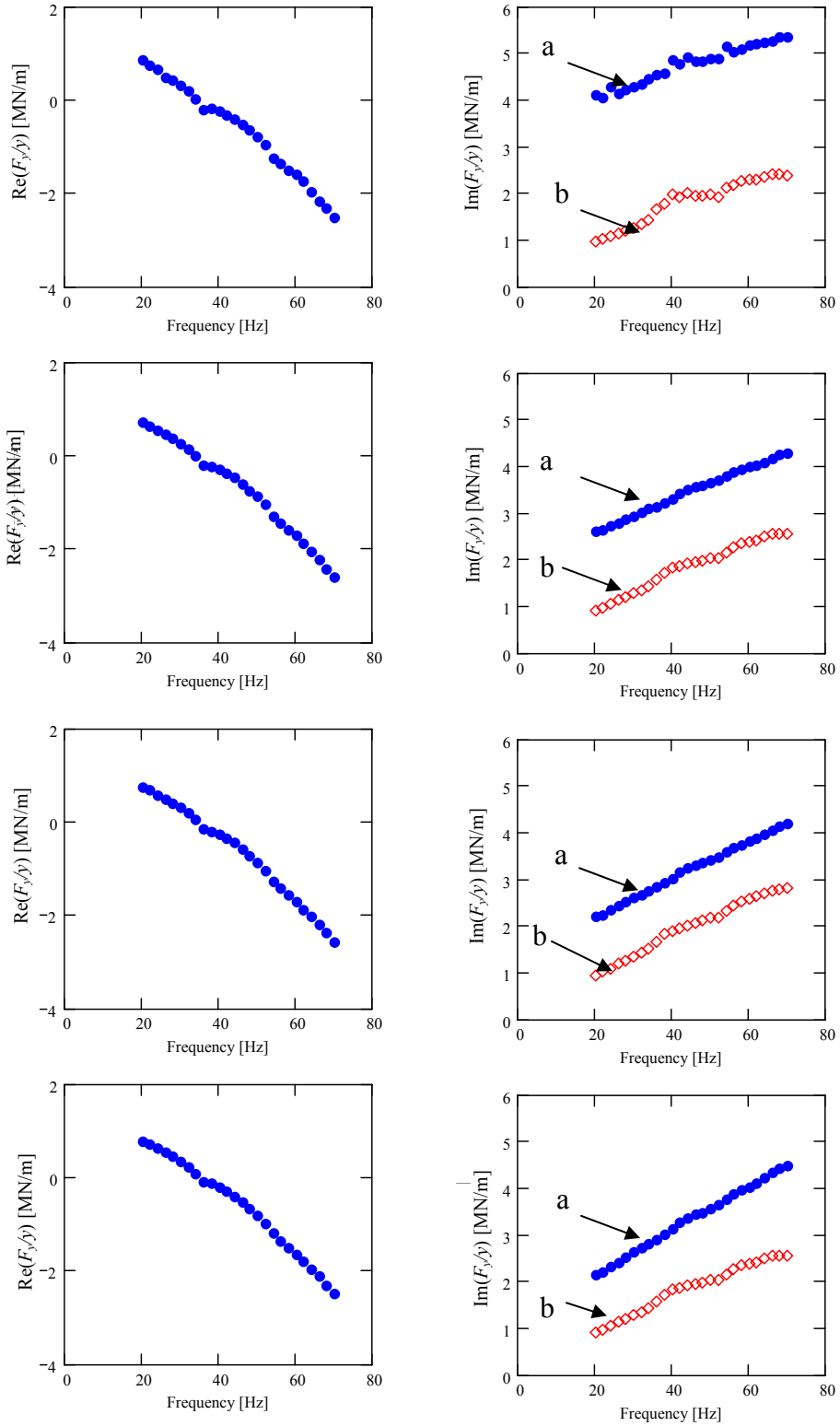from which the frequency averaged squeeze film damper coefficients are extracted. Recall that $\omega C_{seal} = \dfrac{F_\mu}{|\overline{x}|}$, for example. The graphs below correspond to orbital motions of 0.050 mm in amplitude.

$$a \to \mathrm{Im}\left(\frac{\bar{F}_x}{\bar{x}}\right), \quad b \to \mathrm{Im}\left(\frac{\bar{F}_x}{\bar{x}}\right) - \omega C_{seal} - \omega\, C_{rv}$$

Figure D 1 Real and imaginary components of complex dynamic stiffness (F_x/x).(Flow restrictor: 2.8 mm. Dry Friction force: 34 N)

$$a \rightarrow \text{Im}\left(\frac{\bar{F}_y}{\bar{y}}\right), \qquad b \rightarrow \text{Im}\left(\frac{\bar{F}_y}{\bar{y}}\right) - \omega C_{seal} - \omega\ C_{rv}$$

Figure D 2 Real and imaginary components of complex dynamic stiffness (F_y/y).(Flow restrictor: 2.8 mm. Dry Friction force: 34 N)

$$a \to \mathrm{Im}\left(\frac{\overline{F}_x}{\overline{x}}\right), \qquad b \to \mathrm{Im}\left(\frac{\overline{F}_x}{\overline{x}}\right) - \omega C_{seal} - \omega\ C_{rv}$$

Figure D 3 Real and imaginary components of complex dynamic stiffness (F_x/x).(Flow restrictor: 1.1 mm. Dry Friction force: 34 N)

$$a \rightarrow \mathrm{Im}\left(\frac{\bar{F}_y}{\bar{y}}\right), \quad b \rightarrow \mathrm{Im}\left(\frac{\bar{F}_y}{\bar{y}}\right) - \omega C_{seal} - \omega\, C_{rv}$$

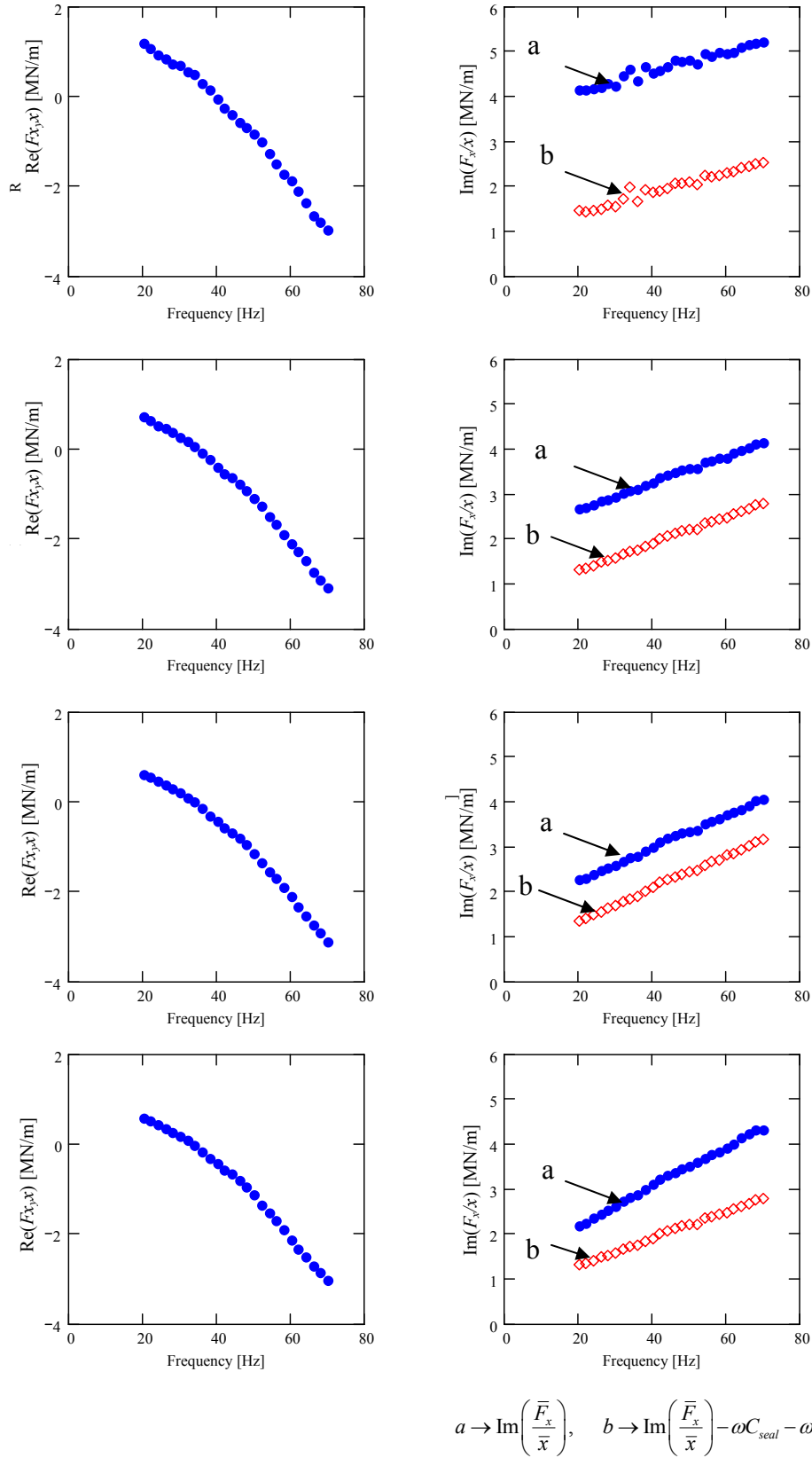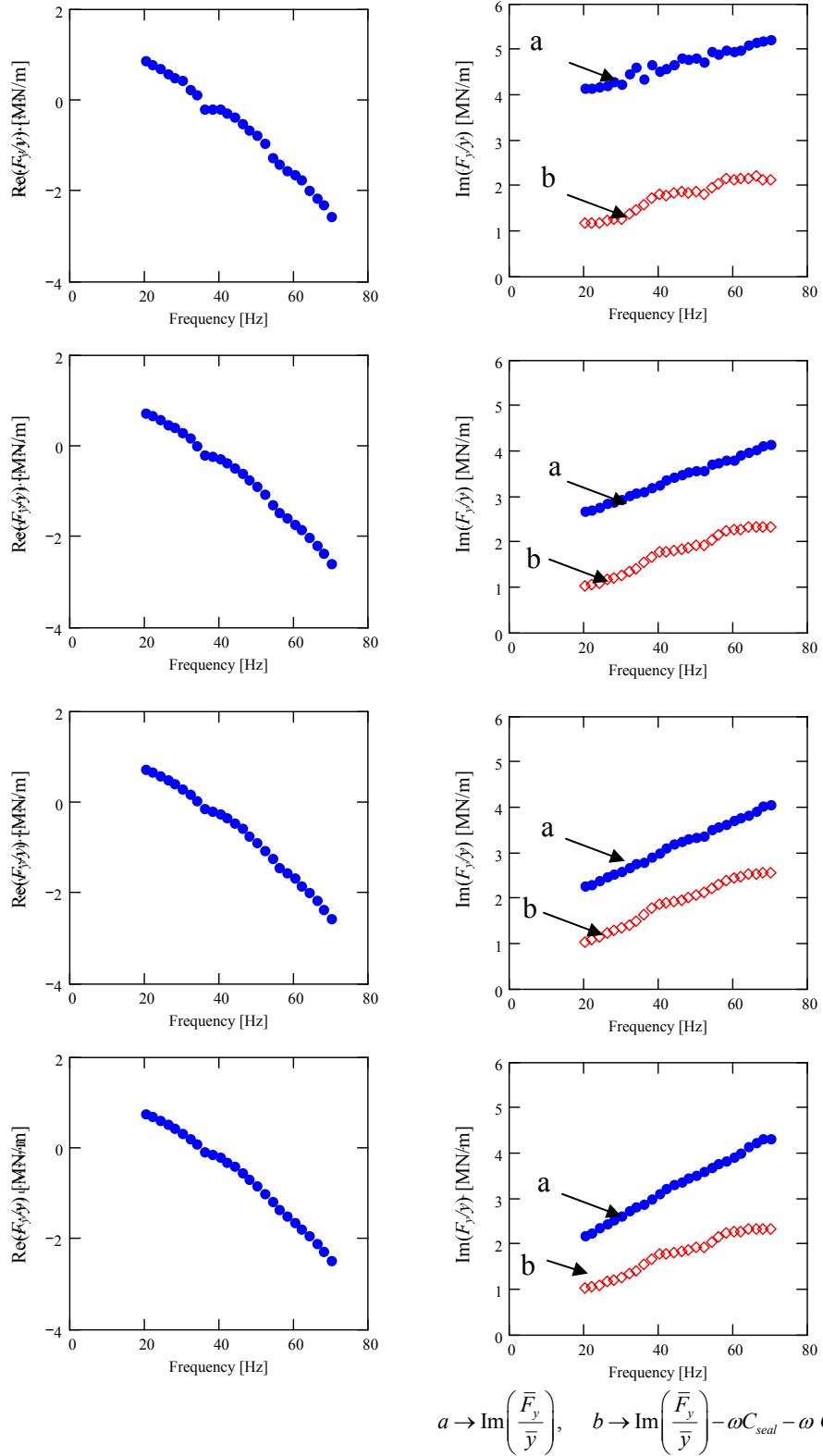**Figure D 4 Real and imaginary components of complex dynamic stiffness (F_y/y).(Flow restrictor: 1.1 mm. Dry Friction force: 34 N)**